nature biotechnology

Article

https://doi.org/10.1038/s41587-026-03077-5

Inducible, split base editors for in vivo cancer functional genomics

Received: 27 January 2025

Accepted: 3 March 2026

Published online: 15 April 2026

Check for updates

Diqiu Ren[1,2,3,15], Shangshang Wang[3,4,15], Keisuke Yamada[1,2,3,5,6,7], Yuqiao Liu[1,2,3], Robert Hapke[3,4,8], Aktan Alpsoy[9], Yugong Ho[10], Canjing Zhang[1,2,3], Yemin Lan[2], Shuo Zhang[2], Joseph P. Milazzo[9], Ruchi Lohia[1,2,3], Kiara N. Berríos[5], Yongjun Li[11], Evan W. Weber[3,8,12,13], Qin Li[10], Christopher R. Vakoc[9], Andy J. Minn[3,4,13,14] ✉, Rahul M. Kohli[2,5,6] ✉ & Junwei Shi[1,2,3,13] ✉

Cancer functional genomics using CRISPR base editors (BEs) holds great promise for molecular characterization and new target discovery. However, traditional BEs, using intact DNA deaminases as mutators, are often constrained by limited control and nonspecific toxicities. Here we developed a small-molecule-controllable system using split-engineered BEs (seBEs). By placing deaminase activity under small-molecule control, seBEs significantly reduced cellular toxicity and enabled robust and inducible in vivo functional genomics screens. High-density seBE genetic screens using ~11,000 single guide RNAs in vitro and ~3,700 single guide RNAs in vivo reveal known and previously unknown loss-of-function and dominant-negative mutations in cancer therapeutic targets. A deeper tiling seBE screen against *Adar1*, a key mediator in cancer immunotherapy, reveals critical residues within functional domains that show no phenotype in vitro but distinctively elicit non-cell-autonomous cancer dependencies in vivo. Overall, our seBE system offers a generalizable, controllable and highly efficient method to systematically identify key residues in cancer functional genomics.

Functional genomics in cancer is a powerful approach for identifying the specific roles of genes critical for tumor development, maintenance and progression[1–4]. These genetic screens link genetic perturbations to the quantitative analysis of cancer phenotypes using deep sequencing, enabling high-throughput dissection of therapeutic target genes. CRISPR functional genetic screens, conducted either in vitro or in vivo, help reveal both cell-autonomous and non-cell-autonomous cancer dependencies[5–12] and have been widely used for target identification at scale[11,12]. Crucial regions or residues of the target gene are typically then identified with follow-up molecular biology or biochemical approaches[13–17]; however, such approaches pose technical challenges with in vivo disease models. Recently, CRISPR base editors (BEs) have expanded functional genomic screens by enabling efficient and high-throughput molecular and mechanistic studies. BEs combine programmable catalytically compromised Cas proteins with cytosine or adenine deaminases to enable targeted nucleotide conversion[18–23].

[1]Department of Cancer Biology, University of Pennsylvania, Philadelphia, PA, USA. [2]Epigenetics Institute, University of Pennsylvania, Philadelphia, PA, USA. [3]Abramson Family Cancer Research Institute, University of Pennsylvania, Philadelphia, PA, USA. [4]Department of Radiation Oncology, University of Pennsylvania, Philadelphia, PA, USA. [5]Department of Medicine, University of Pennsylvania, Philadelphia, PA, USA. [6]Department of Biochemistry and Biophysics, University of Pennsylvania, Philadelphia, PA, USA. [7]Department of Bioengineering, University of Pennsylvania, Philadelphia, PA, USA. [8]Center for Cellular and Molecular Therapeutics, Children's Hospital of Philadelphia, Philadelphia, PA, USA. [9]Cold Spring Harbor Laboratory, Cold Spring Harbor, New York, NY, USA. [10]Department of Genetics, University of Pennsylvania, Philadelphia, PA, USA. [11]Department of Biology, University of Pennsylvania, Philadelphia, PA, USA. [12]Department of Pediatrics, University of Pennsylvania, Philadelphia, PA, USA. [13]Mark Foundation Center for Immunotherapy, Immune Signaling, and Radiation, University of Pennsylvania, Philadelphia, PA, USA. [14]Present address: Immuno-Oncology Program, Memorial Sloan Kettering Cancer Center, New York, NY, USA. [15]These authors contributed equally: Diqiu Ren, Shangshang Wang. ✉e-mail: minna@mskcc.org; rkohli@pennmedicine.upenn.edu; jushi@upenn.edu

BEs specifically enrich for missense mutagenesis, which can generate hypomorphic, dominant-negative or gain-of-function mutations that provide insights beyond those achievable with conventional screening approaches[24–38].

Current BEs rely on intact deaminases that can mutate DNA or RNA independently of Cas9 and single guide RNA (sgRNA) binding, leading to nonspecific toxicity in cells and constraining functional genetic screening, particularly in vivo[39–42]. Cytosine BEs, despite offering extended missense mutagenesis, show higher adverse outcomes than adenine BEs, including detrimental transcriptional responses that subsequently impact editing efficiency[43,44]. Persistent deaminase-mediated nonspecific cellular toxicity often necessitates clonal isolation or de novo cell line generation to ensure stable BE expression[26,28]. Consequently, cytosine BEs are thus far mainly used in screens tolerant of lower editing efficiencies, such as positive selection and fluorescence-activated cell sorting-based approaches[28–32,35], with relatively limited application in negative selection screens[26,37]. Moreover, the cumulative cellular toxicity, reduced gene editing efficiency and lack of inducibility collectively have also restricted BEs, with no successful applications reported to date for in vivo functional genetic screening.

To address these limitations, we developed an in vivo base editing platform using split-engineered BEs (seBEs) whereby the deaminase is split into two inactive parts that can be conditionally reconstituted by small molecules[45]. This approach significantly reduced nonspecific cellular toxicity of BEs relative to intact BEs, while additionally allowing for inducible and tunable base editing with enhanced efficiency. We demonstrate the robust performance of inducible mutagenesis screens using seBEs, identifying both known and previously unknown functional residues in cancer therapeutic targets, including targets that only elicit phenotypes in vivo.

Results

seBEs enable robust inducible gene editing with reduced off-target toxicity

We hypothesized that intact DNA deaminases, acting as mutators, contribute to cellular toxicity and that controllable deaminases could overcome these limitations. In prior work, we demonstrated that the DNA deaminases in BEs can be split into two inactive portions that can be conditionally reconstituted with rapamycin (Rap)[45]. To first investigate BE toxicity, we performed proliferation competition assays with single-copy viral integration to evaluate various BE configurations relevant for functional genetic screening. RN2 cells[46], a genetically engineered mouse model of leukemia, were transduced with one of three constructs: a Cas9 nickase (nCas9), traditional BE4max with an intact evoA1 deaminase or seBE derived from BE4max. Each construct was linked to mCherry, allowing longitudinal tracking of the BE^+ population via flow cytometry relative to nontransduced cells (Fig. 1a,b). We observed that the $nCas9^+$ population remained stable, whereas the intact BE^+ population showed significant and continuous depletion (Fig. 1a), indicating persistent toxicity even under single-copy lentiviral expression. By contrast, the $seBE^+$ population, with or without Rap treatment, remained stable over time (Fig. 1b), indicating that controlling deaminase activity could mitigate proliferation-related cellular toxicity. We confirmed these findings in an independent B16 mouse melanoma model (Supplementary Fig. 1). Cell cycle and cell death analyses further revealed increased apoptosis and reduced S-phase populations in intact BE compared to seBE conditions, consistent with growth-inhibitory toxicity (Fig. 1c and Supplementary Fig. 2).

To further assess BE-associated transcriptional toxicity, we performed RNA sequencing (RNA-seq) on transduced cells in the absence of targeting sgRNAs. Principal component analysis revealed close clustering of nCas9, catalytically mutated intact BE and seBE, which were separated from the intact BE groups in the first principal component (Supplementary Fig. 3a). Differential gene expression analysis showed that intact BE perturbed 1,307 genes relative to nCas9 and 951 genes relative to the catalytic mutant at an absolute $\log_2$ (fold change) (LFC) of >0.5 and adjusted P value of <0.05 (Fig. 1d). By contrast, seBE caused minimal transcriptional perturbation, altering 271 genes relative to nCas9 and 4 genes relative to the catalytic mutant, and with no detectable changes following Rap addition (Fig. 1d and Supplementary Fig. 3b). Consistent with findings from a prior doxycycline-inducible BE system[44], no significant differences in C>U or A<G RNA editing were observed between intact BE and seBE under low-transduction conditions (Supplementary Fig. 4). These findings suggest that the nonspecific cellular toxicity and substantial gene expression perturbation associated with intact BEs limit their effectiveness in functional genetic screening.

Given the potential improvements in off-target toxicities, we next evaluated the efficiency of seBE relative to intact BE in targeting pan-essential genes in cancer cells. We used a two-vector expression strategy with different fluorescence markers, allowing flow cytometry-based tracking of $sgRNA^+/BE^+$ cell populations in proliferation-based competition assays targeting *Cdk1*, *Pcna* and *Myc* as

Fig. 1 | Inducible seBEs show reduced off-target toxicity and higher editing efficiency. a,**b**, Competition-based proliferation assays performed in RN2 cells. **a**, For intact BEs, BE^+ populations were tracked over time using an mCherry coexpression marker. Plotted are the relative BE^+ populations normalized to day 2 after infection ($n = 3$ biological replicates). **b**, For seBEs, C-terminal deaminase–nCas9-expressing cells were tracked by mCherry (mChe), and N-terminal deaminase fragment-expressing cells were tracked by GFP. Vehicle or 1 nM Rap was added at day 2 after infection ($n = 3$ biological replicates). Plotted are the relative $seBE^+$ populations normalized to day 2 after infection. Schematic representations of the intact BE and seBE vector configurations used in these experiments are shown above; Veh, vehicle. Two-way analysis of variance (**$P = 0.0012$). **c**, Cell cycle and apoptotic (sub-G0/G1) analysis of intact BE^+ and $seBE^+$ cells. Cells were analyzed by flow cytometry at 5 days after transduction following BrdU incorporation and DAPI staining ($n = 3$ biological replicates). **d**, MA plots from RNA-seq analysis of gene expression changes in RN2 BE^+ and $seBE^+$ cells from three independent biological replicates. BE^+ and $seBE^+$ cells were sorted at day 5 after infection before RNA-seq. Differential gene expression statistical tests were performed using DESeq2 with a two-sided Wald test; P values were adjusted for multiple comparisons using the Benjamini–Hochberg method. The x axis represents the mean of the read counts of replicates, whereas the y axis shows the LFC calculated by DESeq2. Purple dots indicate genes with a Benjamini–Hochberg-adjusted P value of <0.05 and an absolute LFC of >0.5. Purple dashed lines indicate an absolute LFC of 0.5. evoA1*, a catalytic mutant of evoA1. **e**, Vector configurations of BEs used for competition-based proliferation assays and on-target editing efficiency measurements. The intact BE construct was modified from BE4max. The seBE system comprises two constructs: $seBE_C$ (encoding FK506 binding protein 12 (FKBP12), the C-terminal deaminase fragment, nCas9, two copies of uracil DNA glycosylase inhibitor (UGI) and a puromycin (Puro) resistance marker) and $seBE_N$ (encoding the sgRNA expression cassette, the N-terminal deaminase fragment, the FKBP–Rap-binding domain (FRB) and a GFP reporter). **f**, Competition-based proliferation assays performed in RN2 BE^+ or $seBE_C^+$ cells. $sgRNA^+$ or sgRNA-$seBE_N^+$ populations were tracked over time with a GFP coexpression marker. For intact BE, $sgRNA^+$ populations were normalized to day 3 after infection. For seBE, sgRNA-$seBE_N^+$ populations were normalized to day 0 of vehicle or 1 nM Rap treatment (day 3 after infection; $n = 4$ biological replicates). **g**, Quantification of on-target editing efficiency at eight genomic loci in RN2 cells expressing intact BE or seBE, measured by deep sequencing (Student's t-test, paired, two-sided, ***$P = 0.0002$). Each data point represents one editable cytosine site ($n = 34$). **h**, Schematic workflow of base editing in primary human T cells and flow cytometric comparison of *B2m* knockout efficiency using intact evoA1 or seBE (vehicle or 1 nM Rap) with two independent sgRNAs, measured by loss of HLA surface expression. Results from two donors are shown for all conditions. Statistical comparisons were performed between intact BE-evoA1 and seBE-A3A across sgRNAs and donors using a paired two-sided Student's t-test (**$P = 0.0048$). Error bars smaller than the symbol width are not shown. Data are presented as mean ± s.d.

https://doi.org/10.1038/s41587-026-03077-5

a proxy to evaluate dropout genetic screening performance[47] (Fig. 1e). In intact BE$^+$ cells, nonsense sgRNAs targeting essential genes showed approximately twofold depletion over 10 days relative to the negative control (Fig. 1f). By contrast, seBE$^+$ cells treated with subnanomolar Rap exhibited an enhanced three- to sevenfold depletion, while sgRNA levels remained stable in the vehicle-treated controls over 9 days (Fig. 1f).

A titration of Rap demonstrated dose dependency for gene editing, with detectable activity at concentrations as low as 10 pM (Supplementary Fig. 5a,b). Time-course experiments showed rapid editing kinetics, with ~50% gene editing within 1 h (Supplementary Fig. 6). Treatment with 1 nM Rap, sufficient for robust seBE activity, had minimal impact on endogenous mTOR signaling, as assessed by

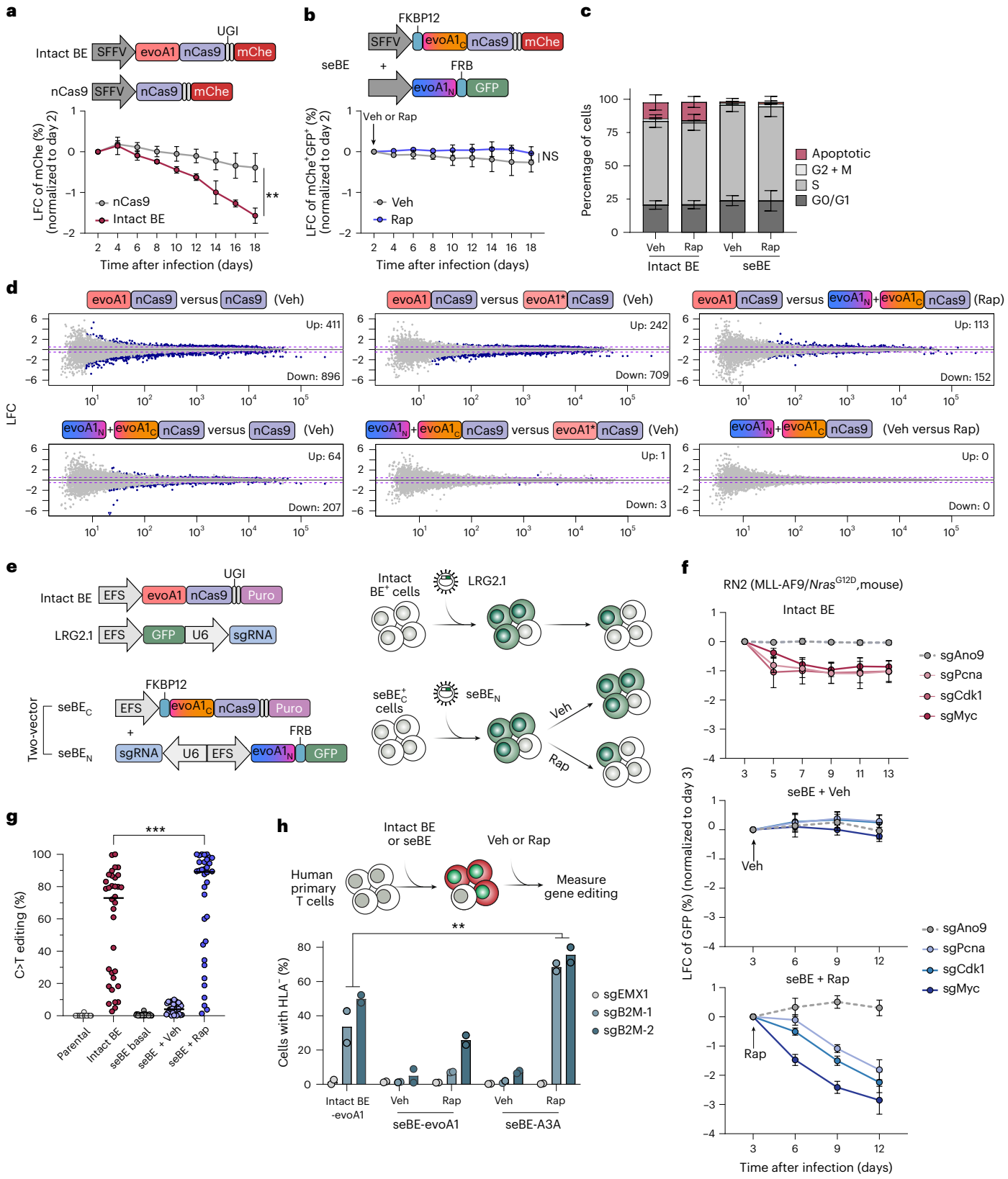

S6K1 phosphorylation[48], with reversion of signaling to baseline within 24 h of Rap removal (Supplementary Fig. 7). Robust inducible editing was further confirmed across eight additional nonessential loci in RN2 cells (Fig. 1g and Supplementary Fig. 8).

We next assessed whether the improved performance of seBE extended to other DNA deaminases and additional cell types, including challenging-to-edit polyploid cancer cells and primary cells. In tetraploid B16 cells, proliferation-competitive assays against essential genes and knockout of the nonessential marker *Cd44* showed that seBE remained effective, with the intrinsically hyperactive deaminase APOBEC3A (A3A) outperforming evoA1 (Supplementary Fig. 9a,b). In primary human T cells, which are typically more refractory to gene editing, we found that seBEs enabled inducible gene editing, with the A3A-based seBE outperforming both the evoA1-based seBE and intact BE, as measured by knockout efficiency of the nonessential *B2m* gene (Fig. 1h and Supplementary Fig. 10). Together, these results support the general applicability of seBEs for controllable, low-toxicity and high-efficiency genome editing across different cellular contexts.

seBE mutagenesis screening reveals known and new loss-of-function mutations in cancer dependencies

As a step toward in vivo applications, we next evaluated seBE performance in in vitro functional genetic screening. We constructed a Cas9 NGG PAM-based tiling sgRNA library targeting the untranslated regions (UTRs), introns and exons of *Myb*, a master transcription factor essential for leukemia[49] (Fig. 2a). Dropout genetic screens were performed in RN2 cells using nuclease-active Cas9 and intact BE or seBE with or without Rap, all at a low multiplicity of infection (MOI). Throughout the screen, >1,000-fold sgRNA representation was maintained, and LFC values were calculated to quantify proliferation effects (Fig. 2a). As expected, positive-control sgRNAs were depleted with nuclease-active Cas9, intact BE and Rap-treated seBE, while minimal selection was observed with vehicle-treated seBE (Fig. 2b and Supplementary Fig. 11a). Due to predominant insertion–deletion mutations, nuclease-active Cas9 showed limited discrimination across MYB, with broad sgRNA depletion. Comparisons between intact BE and seBE highlighted the limitations of intact BE: nonsense sgRNAs showed a narrow LFC range (0.07 to −1.87), whereas Rap-treated seBE showed an expanded dynamic range (0.29 to −4.19), consistent with reduced toxicity and enhanced editing efficiency. In contrast to the no edit, UTR, intron and silent site sgRNAs, a fraction of sgRNAs predicted to create nonsense, splicing site or missense mutations showed Rap-dependent depletion (Fig. 2b).

Given the potential of missense mutations to elicit structure–function relationships, we further focused on missense sgRNAs targeting *Myb* (Fig. 2b,c). Across all missense sgRNAs, the average depletion was 2.8-fold higher with seBEs (LFC ratio of 1.49) than with intact BEs (Supplementary Fig. 11b). Missense sgRNAs targeting the three DNA-binding domains (DBDs) and the transcription activation domain of MYB were preferentially depleted, in contrast to the more homogenous depletion observed with nonsense sgRNAs (Fig. 2c and Supplementary Fig. 12a). To validate these findings, we selected three missense sgRNAs (sgMyb-99, sgMyb-151 and sgMyb-152) that target different DBDs and confirmed their antileukemia effects (Fig. 2d and Supplementary Fig. 13a). On-target sequencing confirmed 55–65% editing efficiency, generating specific mutations in DBD2 and DBD3 (Fig. 2e and Supplementary Fig. 14). Immunoblotting showed reduced protein stability in sgMyb-99 compared to controls (Fig. 2f). Although structural analysis using MYB–DNA cocrystal structures (PDB 1MSE) indicated that these mutations were proximal to, but not directly involved in, DNA interaction sites (Fig. 2g and Supplementary Fig. 15), further electrophoretic mobility shift assays using recombinant proteins containing mutations nominated by sgMyb-99 (E99K or D100N) showed reduced DNA binding to a canonical MYB motif, suggesting that these residues indirectly influence DNA interactions (Fig. 2h).

To further validate the utility of seBE functional genomics screening, we expanded our in vitro studies to include additional high-value leukemia therapeutic targets, BRD4 and SMARCA4, chromatin regulators with multiple essential domains critical for leukemia maintenance[50–53]. As expected, missense tiling screening identified hot spots within functional domains (Fig. 2i, and Supplementary Figs. 12b,c and 16a). For BRD4, missense sgRNAs targeting the two bromodomains (BDs) were preferentially depleted, with sgBrd4-144 (D144/D145 in BD1) and sgBrd4-444 (M443/A444 in BD2) among the top hits (Supplementary Figs. 13b and 16a). These sgRNAs targeted residues involved in acetylated histone lysine or JQ1 binding, as supported by either structure or AlphaFold3 predictions[51] (Supplementary Fig. 16b,d,e). For SMARCA4, sgSmarca4-973 and sgSmarca4-1309, targeting the ATPase and SnAC domains, respectively, were among the top depleted missense sgRNAs (Fig. 2i and Supplementary Fig. 13c). Proliferation-based competition assays confirmed that these sgRNAs inhibited leukemia proliferation (Fig. 2j and Supplementary Fig. 16c). Of note, sgSmarca4-973, predicted to generate R973Q near the ATPase domain (Fig. 2k), showed stronger depletion than nonsense or splice site sgRNAs (Fig. 2j). In overexpression assays to evaluate this mutant, ectopic overexpression of wild-type SMARCA4 had minimal impact, whereas R973Q phenocopied a known dominant-negative ATPase-defective mutant K785R[53] (Fig. 2l), suggesting a potential dominant-negative effect. Together, these results highlight that missense sgRNA seBE tiling screening can identify known functional residues and uncover new loss-of-function and dominant-negative mutations.

Optimized seBE toolkits and improved LASER missense sgRNA design

To broaden the applicability of seBEs for functional genetic screening, we next diversified and optimized the inducible components. In addition to Rap-mediated FKBP12–FRB heterodimerization[54], we explored

Fig. 2 | seBE tiling mutagenesis screen design. a, Schematic workflow of tiling library design and mutagenesis screening; D3, day 3; D15, day 15. **b**, Scatter plot of average sgRNA LFC values of two independent biological replicates ($n = 2$) for sgRNAs classified by predicted editing outcome. Each dot represents the average LFC across replicates. The number of sgRNAs in each category is shown above each label. **c**, Scatter plot of *Myb* tiling screening results for predicted missense sgRNAs, plotted against the target sites in the protein sequence ($n = 2$ biological replicates); aa, amino acids. **d**, Competition-based proliferation assays performed in RN2 seBE$^+$ cells ($n = 4$ biological replicates). **e**, Validation of sgMyb-99 targeting after 24 h of vehicle or Rap treatment. Sequencing results are visualized as heat maps, with dashed boxes indicating amino acid mutations. Deep sequencing was performed once. **f**, Western blotting of MYB and GAPDH levels in whole-cell lysates of RN2 seBE$^+$ cells treated with Rap for 24 h. A representative western blot is shown from three biological experiments. **g**, View of the mouse MYB DBD 2 with DNA helix (PDB 1MSE). sgMyb-99-targeted residues are labeled in red, and residues potentially involved in polar contacted are shown in green. **h**, Binding of purified DBDs to oligonucleotide probes measured by electrophoretic mobility shift assay. **i**, Scatter plot of average LFC values from *Smarca4* seBE tiling results for missense sgRNAs ($n = 2$ biological replicates). **j**, Competition-based proliferation assays performed in RN2 seBE$_C^+$ cells ($n = 3$ biological replicates). Statistical significance between sgSmarca4-973 and sgSTOP was determined by two-way analysis of variance (*$P = 0.047$). **k**, View of the mouse SMARCA4 SNF2 and helicase domains with ATP predicted by AlphaFold. Residues are colored by average LFC values from mutagenesis screening. R973 and R974 are labeled in red. **l**, Effects of lentiviral overexpression of SMARCA4 variants on RN2 cell growth in the presence of endogenous wild-type SMARCA4. Wild-type or mutant *Smarca4* cDNAs were expressed from an EFS-P2A–mCherry vector, and changes in mCherry$^+$ cell frequency were used to quantify growth rates ($n = 3$ biological replicates). Statistical significance between R973Q and wild-type was determined by two-way analysis of variance (****$P < 0.0001$). Error bars smaller than the symbol width are not shown. Data are presented as mean ± s.d.; EV, empty vector.

https://doi.org/10.1038/s41587-026-03077-5

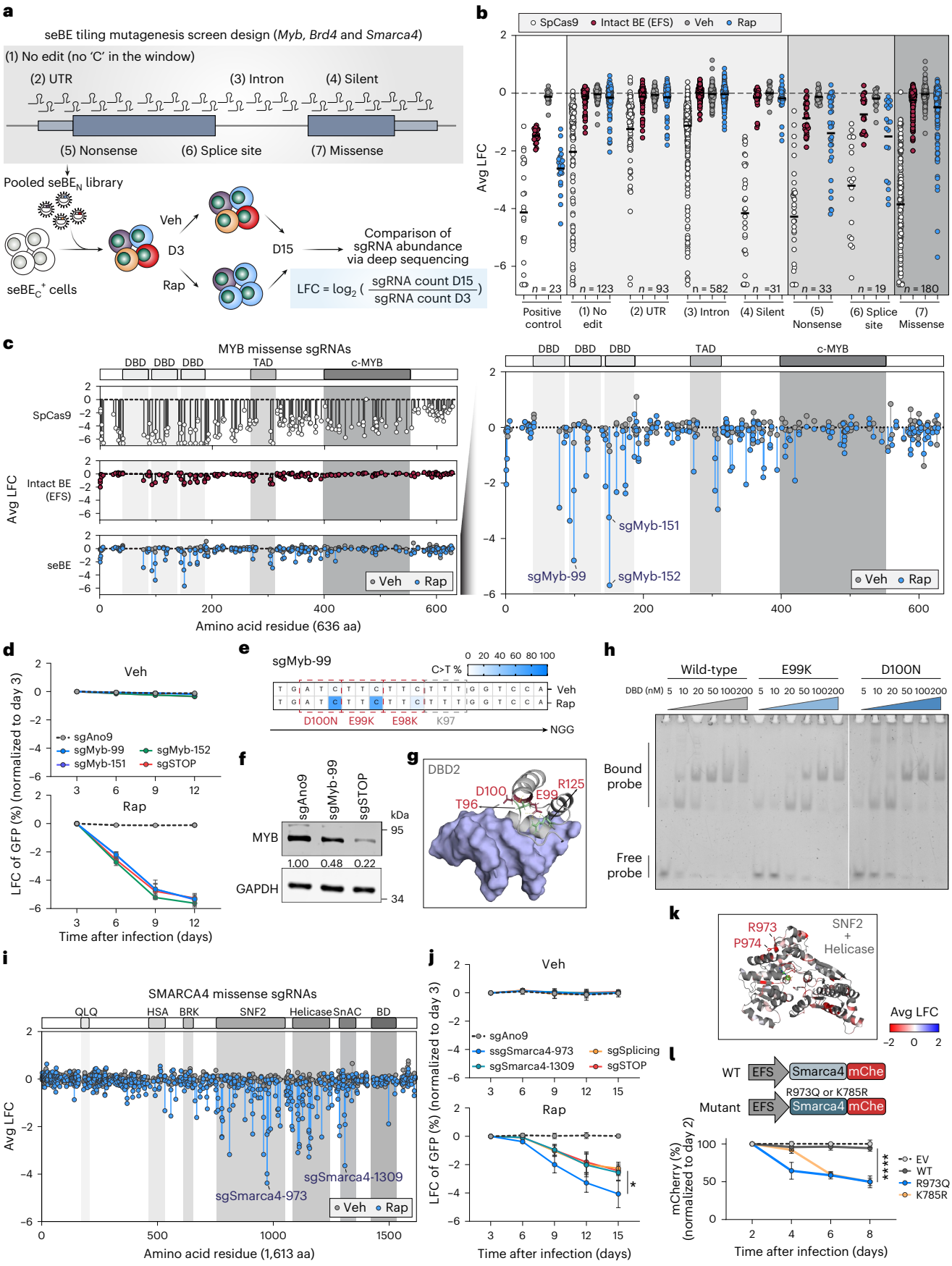

https://doi.org/10.1038/s41587-026-03077-5

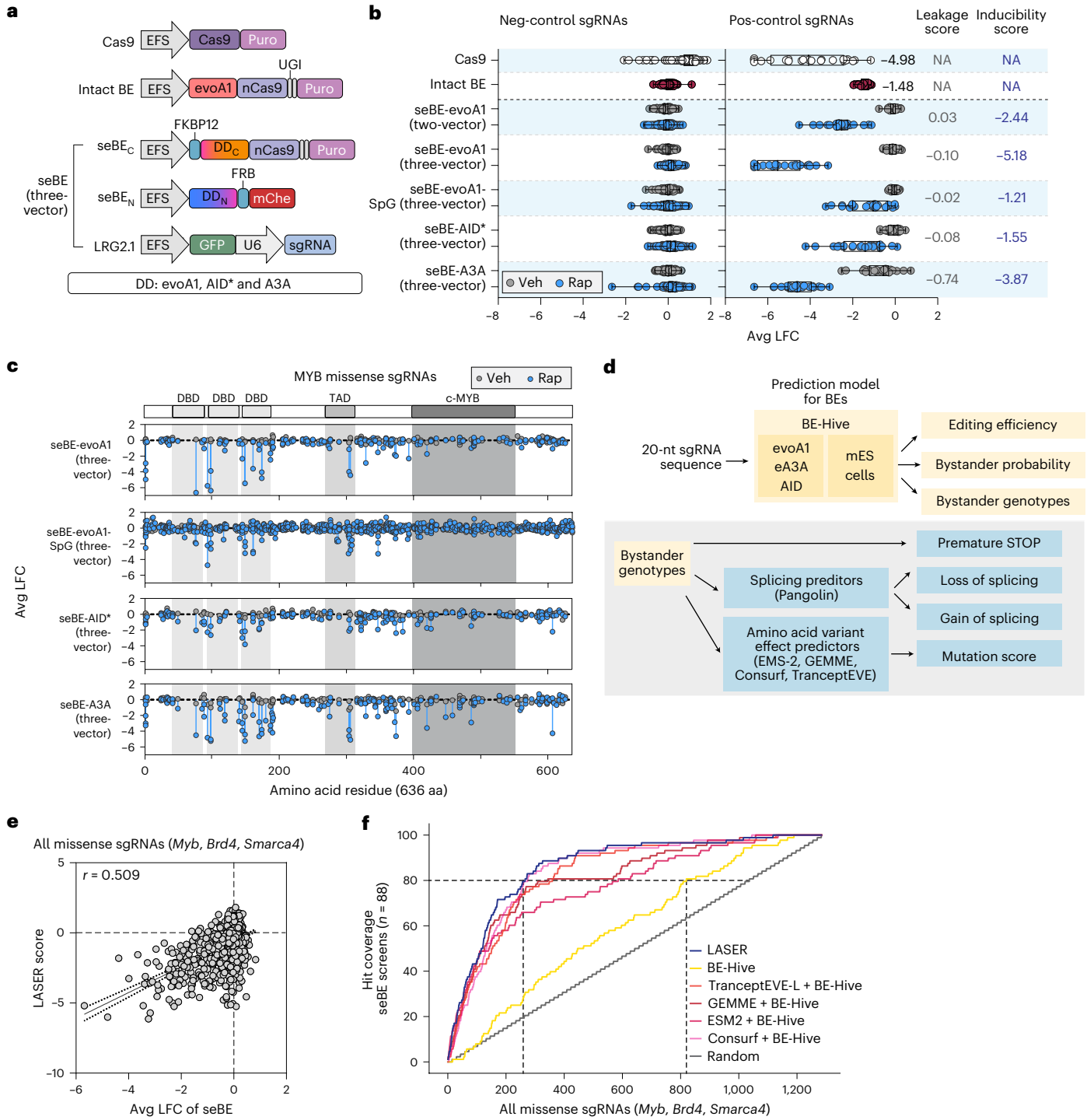

Fig. 3 | Expanded seBE toolkits and LASER missense sgRNA design. a, Vectors used for Cas9- and BE-based mutagenesis screenings. In the three-vector system, the C-terminal DNA deaminase fragment is coexpressed with nCas9 and selected with puromycin, the N-terminal DNA deaminase fragment is coexpressed with an mCherry reporter, and sgRNAs are expressed from the LRG2.1 vector with a GFP reporter. Cas9$^+$ or BE$^+$ cell populations were enriched by puromycin selection and/or flow cytometric sorting based on GFP and mCherry expression before genetic screening; DD, DNA deaminase. **b**, Scatter plot of average sgRNA LFC values for negative (Neg) controls and positive (Pos) controls from each screen. The inducibility scores of seBEs were calculated by comparing the average LFC of positive-control sgRNAs between vehicle- and Rap-treated groups. The leakage scores of seBEs were evaluated as the average LFC of positive-control sgRNAs in the vehicle-treated group relative to the average LFC of negative-control sgRNAs. Editing activity of SpCas9 and intact BE was calculated by comparing the average LFC of positive-control sgRNAs to that of negative-control sgRNAs. Positive-control sgRNAs were prevalidated to target pan-essential genes or established leukemia dependencies, whereas negative-control sgRNAs targeted nonessential genes containing at least one editable cytosine within the BE editing window ($n = 2$ biological replicates); NA, not applicable. **c**, Scatter plot of *Myb* tiling results using seBE constructs with altered configurations and missense sgRNAs, plotted against the target sites in the protein sequence ($n = 2$ biological replicates). **d**, Schematic of incorporation of predictions from different language models and protein evolutionary conservation profiles for guiding improved sgRNA design principles; nt, nucleotides; mES cells, mouse embryonic stem cells. **e**, Correlation between the average LFC values from the mutagenesis screening and LASER prediction score (simple linear regression, two-tailed, $P < 0.0001$). **f**, Comparison of effective sgRNA selection between the BE-Hive model, LASER and random selection. The dashed lines indicate the library size based on each model for 80% effective sgRNA coverage.

two alternative small-molecule-based approaches: a nonimmunosuppressive rapalog A/C-mediated FRB mutant system[55] and an abscisic acid-mediated ABI-PYL1 system[56]. Using HEK293T and K562 reporter cell lines expressing a destabilized form of green fluorescent protein (d2GFP), where a nonsense mutation in d2GFP serves as a proxy for editing efficiency, we found that both systems showed inducible base editing, although our original Rap-based system exhibited higher overall editing efficiency (Supplementary Fig. 17a–h). We further validated rapalog- and abscisic acid-based seBEs in targeting pan-essential genes, confirming inducible editing and improved gene perturbation (Supplementary Fig. 17i,j). Given Rap's status as an economical and clinically safe drug, although encouraged by the availability of options, we prioritized the Rap-based seBE system for subsequent studies, especially for in vivo genetic screening.

We next optimized and assessed additional seBE components, including vector configuration, Cas9 and deaminase (Fig. 3a). Inducibility was assessed by comparing LFC values of pan-essential sgRNAs between vehicle and Rap treatment, while leakage was measured relative to negative control (Fig. 3b). Dividing seBE components into three vectors doubled inducibility while maintaining baseline leakage (Fig. 3b). Replacing nCas9 with the PAM-relaxed nSpG expanded targeting scope from NGG to NG and enhanced screening resolution but reduced inducibility, consistent with reduced intrinsic activity of nSpG[57] (Fig. 3b,c). Substituting evoA1 with a hyperactive deaminase A3A and a hyperactive AID variant (AID*)[45,58,59] further altered performance in complementary ways: seBE-A3A showed strong inducibility with noticeable leakage, whereas seBE-AID* showed modest inducibility but minimal leakage (Fig. 3b). Both variants identified additional hot spot mutants, likely attributed to A3A's increased deaminase activity and the enhanced processivity of AID* on DNA[60] (Fig. 3c). These results highlight the modularity and adaptability of seBEs for customized functional genomics applications.

Last, to position seBEs for in vivo screening, we optimized sgRNA design to enrich effective missense sgRNAs. Our initial tiled screening revealed that ~10% of the missense sgRNAs exhibited strong depletion, comparable to nonsense sgRNAs (LFC < −1, $P < 0.001$). As in vivo settings with limited cell numbers could benefit from compacted libraries, we investigated if sequence features could predict missense sgRNA efficacy. We first assessed BE prediction models and found that BE-Hive[61] closely captured seBE-edited cytosines and frequencies (Supplementary Fig. 18). We then used ESM-2, GEMME, Consurf and TranceptEVE models[62–67] to calculate variant effect prediction scores for missense sgRNA-induced amino acid alternation. These scores were integrated with BE-Hive editing profiles to generate a combined loss-of-function score, which we termed large language model/machine learning-assisted seBE missense sgRNA (LASER) score (Fig. 3d). Retrospective analysis showed a positive correlation between LASER score and experimental LFC values (Fig. 3e and Supplementary Fig. 19a). Defining hits as sgRNAs with a low LFC (z score of <−1.96), the top 20% of LASER-ranked sgRNAs captured 80% of experimental hits in accumulation curve analysis (Fig. 3f). By contrast, BE-Hive alone required selecting 61–77% of all possible sgRNAs to achieve similar coverage, only slightly better than random (Fig. 3f and Supplementary Fig. 19b,c). These results suggest that LASER can effectively prioritize missense sgRNAs and, combined with the modular seBE system, can enhance the efficiency of functional genomics screens using BEs.

LASER-guided inducible seBE screening of non-cell-autonomous dependencies in vivo

In vivo functional genomics using mouse cancer models provides a physiologically relevant and crucial preclinical platform for therapeutic target identification and validation. Having established the enhanced and inducible seBE system, we aimed to evaluate its performance for in vivo functional genetic screening using the B16 melanoma model, a commonly used model for studying cancer immunotherapy targets[5,9,68,69]. seBE-A3A$^+$ B16 cells were xenografted into immunocompetent mice, followed by intraperitoneal Rap administration to activate the seBE within established tumor cells. A single dose of Rap achieved robust base editing (70–80%) at neutral genomic loci, with a modest additional increase after a second dose (Fig. 4a). Because Rap can inhibit mTOR and modulate antitumor immunity, we profiled tumor-infiltrating immune populations. Editing at a neutral *Ano9* site caused minimal changes across major myeloid and lymphoid subsets (Fig. 4b and Supplementary Figs. 20 and 21). These results suggest that the seBE could enable effective inducible in vivo genetic studies of tumor and immune cell interactions.

To apply seBEs to screening in vivo, we selected 35 genes implicated in cancer immune function, including regulators of interferon (IFN) and tumor necrosis factor (TNF) signaling, epigenetic modification, antigen processing, ubiquitination and the NF-κB pathway[5,8,9,70,71]. Although prior knockout studies have linked these genes to altered antitumor responses, the specific residues essential for in vivo phenotypes remain undefined. Using LASER, we designed a compact sgRNA library containing ~1,800 sgRNAs, including positive- and negative-control sgRNAs. seBE-A3A$^+$ B16 cells, transduced with the pooled sgRNA library at a low MOI, underwent parallel screening in vitro and in vivo. In vitro screening used continuous Rap treatment, whereas in vivo screening received two Rap doses starting 3 days after transplantation to

Fig. 4 | LASER-guided inducible seBE screening of cancer immune genes in vivo. a, Quantification of inducible on-target gene editing efficiency of the seBE system in the B16 melanoma model. Left: schematic workflow in which sgAno9-transduced seBE-A3A$^+$ B16 cells were xenografted into immunocompetent mice, followed by treatment with vehicle or the indicated doses of Rap at either day 3 (1 dose) or days 3 and 6 (2 dose) after implantation. Tumor cells were isolated at day 15 after implantation and subjected to deep sequencing of the targeted locus. Middle: heat map showing on-target editing efficiencies. Right: corresponding quantification bar graph ($n = 4$ mice per condition); i.p., intraperitoneal. **b**, Analysis of tumor-infiltrating immune cell populations in B16 tumors. Flow cytometry was performed on tumor samples collected at day 15 after implantation following vehicle ($n = 7$ mice) or two-dose Rap ($n = 9$ mice) treatment. Each dot represents an individual mouse (two-sided Mann–Whitney test); T_{reg}, regulatory T cells; NK, natural killer cells; Mono, monocytes; Mac, macrophages; M1, M1 macrophages; M2, M2 macrophages; cDC, conventional dendritic cells; TAN, tumor-associated neutrophils. **c**, Schematic workflow of in vitro and in vivo seBE genetic screening of 35 cancer immune genes using a LASER-guided compact sgRNA library. Tumor cells were collected at day 15 after implantation for in vivo screens and at day 15 in culture for in vitro screens, followed by deep sequencing-based quantification of sgRNA representation. **d**, Scatter plot of in vitro and in vivo seBE tiling screen results showing differential LFC, calculated by comparing vehicle- ($n = 5$ mice) and Rap-treated ($n = 10$ mice) conditions. Negative-control sgRNAs are shown as white dots, and positive-control sgRNAs targeting pan-essential genes are shown as dark gray dots. In vivo-biased hits were identified using the MAGeCK test with negative-control normalization, using one-sided tests for enrichment (P_{high}) or depletion (P_{low}) with raw $P < 0.01$, Benjamini–Hochberg FDR < 0.1 and absolute differential LFC > 1, and are highlighted in blue (44 missense sgRNAs enriched) or red (45 missense sgRNAs depleted). The top ten enriched and depleted in vivo missense sgRNAs are labeled. **e**, Scatter plots of in vitro and in vivo seBE screening results using LASER-designed sgRNAs for selected genes (*Kirrel1*, *Nf2*, *Jak1*, *Stub1*, *Rnf31*, *Arid1a*, *Arid2*, *Ep300* and *Pbrm1*). Differential LFC values between Rap- and vehicle-treated conditions are plotted against target positions along the protein sequence. sgRNAs targeting splice sites or predicted to generate premature stop codons are shown as references for genetic knockout. Missense sgRNAs identified as hits from **d** are highlighted in red (depleted) or blue (enriched). Box plots show the LFC values of nonsense and splicing sgRNAs. The center line indicates the median, boxes represent the 25th–75th percentiles, and whiskers extend to the minimum and maximum nonoutlier values. Error bars smaller than the symbol width are not shown. Data are presented as mean ± s.d.; NS, not significant; Igl, immunoglobulin-like.

https://doi.org/10.1038/s41587-026-03077-5

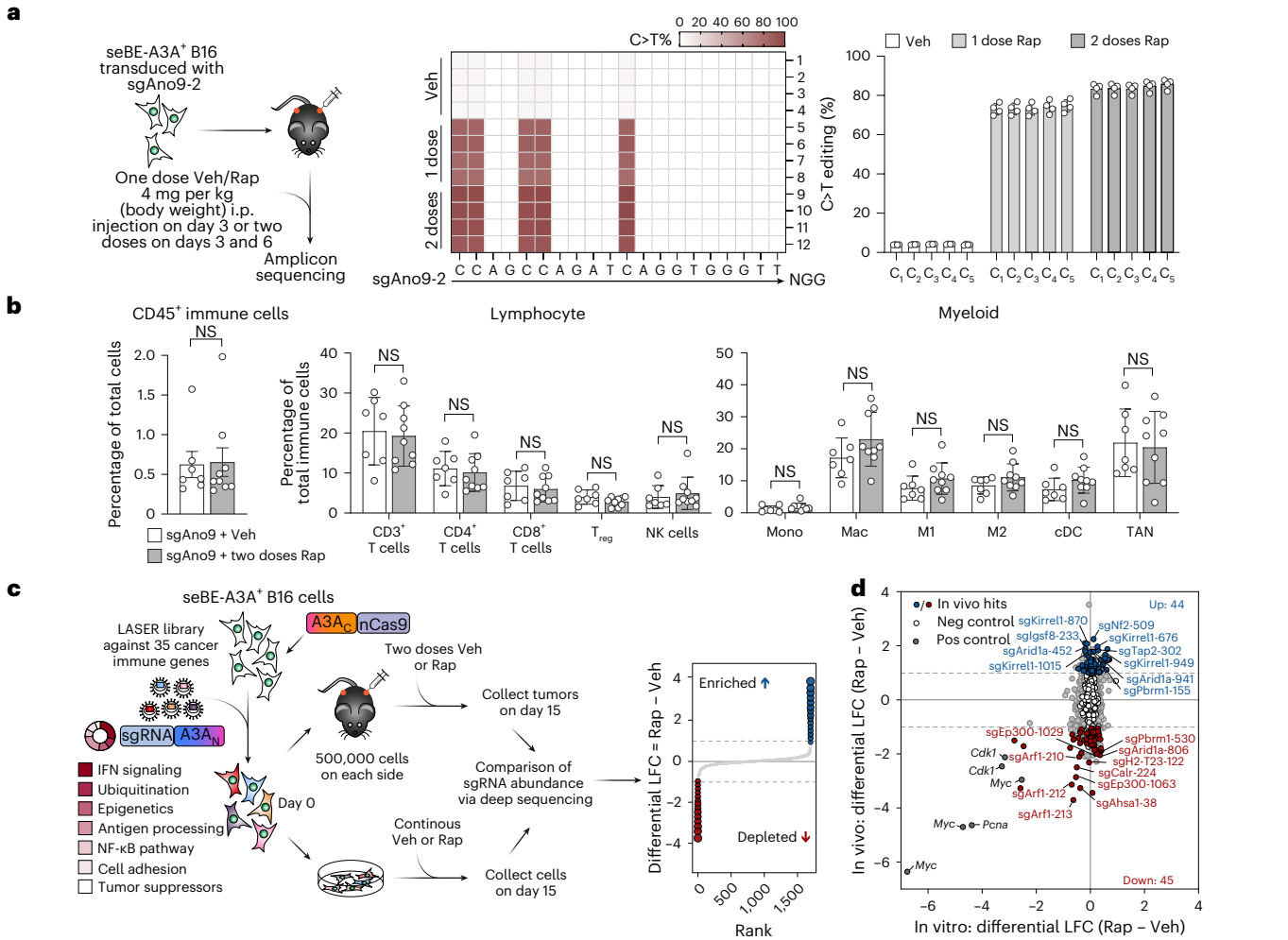

maximize base editing. Cells were collected at day 3 after transduction as baseline, at day 15 after sorting for in vitro analysis and at day 15 after transplantation for in vivo analysis. sgRNA LFC values were calculated relative to the baseline, and differential LFC values were derived by comparing Rap- and vehicle-treated groups (Fig. 4c).

Analysis of positive-control sgRNAs confirmed minimal background editing without Rap and robust Rap-dependent editing in vitro and in vivo (Supplementary Fig. 22a,b). Across the 35 targeted genes, most missense sgRNAs displayed no significant changes in vitro; meanwhile, a fraction exhibited positive or negative selection specifically in vivo (Fig. 4d), aligning with the reported in vivo selective roles for the targets in antitumor immunity. Using $P < 0.01$ and an absolute differential LFC of >1, we identified 89 of 1,417 missense sgRNAs as high-confidence in vivo hits (Fig. 4d). Mapping to the corresponding protein domains revealed preferential in vivo selection of sgRNAs within annotated functional regions (Fig. 4e and Supplementary Fig. 23).

We examined patterns in genes by functional category. Among tumor suppressors, missense sgRNAs targeting the immunoglobulin-like domain of KIRREL and the FERM domain of NF2 were strongly enriched in vivo, similar to nonsense sgRNAs (Fig. 4e). However, a minority of missense sgRNAs dropped out, suggesting highly residue-specific functional switches in these canonical tumor suppressors. For genes whose deletion enhances antitumor immune sensitivity, including antigen processing regulators (*Tap1*, *Tap2* and *Calr1*), ubiquitin ligases (*Rnf31* and *Stub1*), NF-κB pathway components (*Tab2* and *Rela*) and IFN/TNF signaling regulators (*Jak1*, *Stat1*, *Ifngr1*, *Ifngr2*, *Ripk1* and *Ptpn2*), the screen identified critical residues underlying known functions and nominated residues associated with potential resistance. Consistent with prior findings on context-dependent IFN and TNF signaling effects[69,72], residues within these regulators could display divergent immune functions (Fig. 4e and Supplementary Fig. 23). Among the epigenetic regulators *Arid1a*, *Arid2*, *Ep300* and *Pbrm1* (refs. 9,70,73), seBE screening identified discrete and essential residues within BDs of PBRM1, DBDs of PBRM1 and ARID1A, the HAT domain of EP300 and several candidate sites within unannotated or unstructured regions (Fig. 4e). Collectively, these findings demonstrate that seBE screening not only pinpoints critical residues within genes governing antitumor immunity, thereby nominating potential therapeutic intervention sites, but also uncovers context-dependent residues with opposing functional outputs, providing insights to prompt added mechanistic investigation.

seBE tiling mutagenesis screening reveals critical residues of ADAR1

To more thoroughly illustrate how coupled in vitro and in vivo screening can offer rich mechanistic insights into immunotherapeutic targets, we selected *Adar1* for higher-resolution tiled screening in B16 tumors. ADAR1, an adenosine deaminase, transforms adenosine into inosine in double-stranded RNA (dsRNA), modulating immune responses by limiting dsRNA sensing and reducing inflammation and IFN responses[74–77]. Mutations disrupting ADAR1 are also linked to autoimmune diseases such as Aicardi–Goutières syndrome and dyschromatosis symmetrica hereditaria[78–82]. Although *Adar1* had been recently identified as an in vivo-specific immunotherapeutic target in the B16 model[6], the critical domains and residues mediating tumor immune phenotypes remain unstudied. We thus constructed an sgRNA library tiling across *Adar1*, encompassing 1,689 all possible NGG sgRNAs covering its two Z-DBDs, three dsRNA binding domains (dsRBDs) and the adenosine deaminase catalytic domain.

Parallel in vitro and in vivo screens were performed with and without Rap. Comparative analysis revealed that a fraction of nonsense, splicing changes and missense sgRNAs were depleted in vivo but unchanged in vitro, aligning with previous findings that *Adar1* knockout specifically drives tumor immunity in vivo without affecting in vitro growth[6] (Fig. 5a,b and Supplementary Fig. 24a,b). Retrospectively applying LASER to the in vivo seBE-A3A ADAR1 screening showed positive correlation between LASER scores and experimental LFC values, further validating LASER's ability to predict loss-of-function missense sgRNAs (Supplementary Fig. 25a,b).

Mapping depleted missense sgRNAs revealed hot spots in dsRBD1, dsRBD3 and the deaminase domain (Fig. 5b). To integrate structural context with our seBE screening data, we used AlphaFold3 to model ADAR1 with a dsRNA substrate (Supplementary Fig. 26a). We annotated ADAR1 amino acids with sgRNA LFC scores and superimposed these scores on the predicted structure (Fig. 5c), highlighting the strong depletion clustered in dsRBD1 and dsRBD3 specifically at dsRNA interaction interfaces and within the catalytic domain, including near the inositol hexakisphosphate and zinc-binding sites[83] (Fig. 5b,c and Supplementary Fig. 26b,c). sgAdar1-983 and sgAdar1-950, among the

Fig. 5 | In vivo seBE tiling mutagenesis screening reveals critical residues of ADAR1. a, Scatter plot of in vitro and in vivo seBE *Adar1* tiling screen results showing differential LFC (Rap versus vehicle). Negative controls are shown in white, and positive controls targeting pan-essential genes are shown in gray. In vivo-biased hits were identified using MAGeCK with negative-control normalization (one-sided tests for enrichment or depletion with raw $P < 0.01$, Benjamini–Hochberg FDR < 0.1 and | differential LFC | > 1). Enriched sgRNAs ($n = 25$) are highlighted in blue, and depleted sgRNAs ($n = 50$) are highlighted in red. Top hits are labeled ($n = 2$ biological replicates). **b**, Scatter plots of missense sgRNAs from in vitro and in vivo tiling screens. Differential LFCs (Rap versus vehicle) are plotted against amino acid position. Missense sgRNAs identified as hits from **a** are highlighted in red or blue. **c**, Structure view of the AlphaFold-predicted mouse ADAR1 catalytic domain bound to dsRNA. Residues are colored by average LFC values from the in vivo screen. A zinc ion and inositol hexakisphosphate (IP_6), buried within the enzyme core, are shown based on crystal structure of the human ADAR2 catalytic domain (PDB 1ZY7 and 5HP2). A second zinc-binding site is located on the protein surface. **d**, Proliferation competition assays in seBE$^+$ B16 cells transduced with the indicated *Adar1* sgRNAs ($n = 3$ biological replicates; two-sided Student's *t*-test; $^{**}P < 0.01$, $^{***}P < 0.001$; significant *P* values from the left to the right are 4.8×10^{-6}, 0.0003, 0.0008, 2.3×10^{-6}, 0.0002, 1.5×10^{-5}, 1.8×10^{-5}, 0.0009, 0.0002, 1.0×10^{-7}, 5.5×10^{-5}, 0.0001, 3.0×10^{-5}, 0.0034 and 0.0008); NT, nontreated vehicle control. **e**, Validation of on-target editing profiles for individual *Adar1* sgRNAs. Cells were treated with vehicle or Rap for 24 h, followed by deep sequencing. Heat maps show editing outcomes, with dashed boxes indicating predicted amino acid substitutions. The asterisk indicates a stop codon. **f**, Tumor growth in immunocompetent mice transplanted with B16 tumors transduced with the indicated sgRNAs. Mice were treated with vehicle or a dose of Rap (4 mg per kg (body weight)) at day 3 after implantation (for sgAdar1-925, $n = 5$ mice per group; for sgSTOP and sgAdar1-950, $n = 5$ vehicle-treated and $n = 10$ Rap-treated mice; two-sided mixed-effects model; $^{***}P = 0.0006$ and $^{****}P < 0.0001$; data are presented as mean ± s.e.m.). **g**, Survival of mice from **f** (log-rank test; $^{***}P = 0.0004$ and $^{****}P < 0.0001$). **h**, Percentage of seBE$^+$ cells within B16 tumors after a single Rap dose, as in **f**. Each dot represents an individual mouse (for sgAdar1-925 and sgSTOP, $n = 5$ mice; for sgAdar1-950, $n = 4$ mice; two-sided Mann–Whitney test; $^{*}P = 0.0159$ and $^{**}P = 0.0079$). **i**, Tumor growth in mice transplanted with B16 tumors derived from pooled single-cell clones from the indicated *Adar1* sgRNAs. Eight independently validated clones per sgRNA were pooled (for sgAno9 and sgAdar1-950, $n = 10$ mice; for sgAdar1-925 and sgSTOP, $n = 15$ mice; two-sided mixed-effects model; $^{****}P < 0.0001$; data are presented as mean ± s.e.m.); s.c., subcutaneous. **j**, Survival of mice from **i** (log-rank test; $^{****}P < 0.0001$). **k**, Analysis of tumor-infiltrating immune cell populations in B16 tumors. seBE$^+$ B16 cells transduced with sgAno9 ($n = 6$ mice) or sgAdar1-950 ($n = 8$ mice) were implanted into mice, followed by a single Rap dose. Flow cytometry was performed on tumor samples collected at day 15 after implantation. Each dot represents an individual mouse (two-sided Mann–Whitney test; $^{***}P = 0.0007$). **l**, RNA editing levels at the 3′ UTR of the *DCAF16* locus in cells expressing wild-type or mutant ADAR1. RNA was isolated and subjected to nanopore sequencing to quantify editing levels ($n = 2$ biological replicates). Error bars smaller than the symbol width are not shown. Unless otherwise specified, data are presented as mean ± s.d.

https://doi.org/10.1038/s41587-026-03077-5

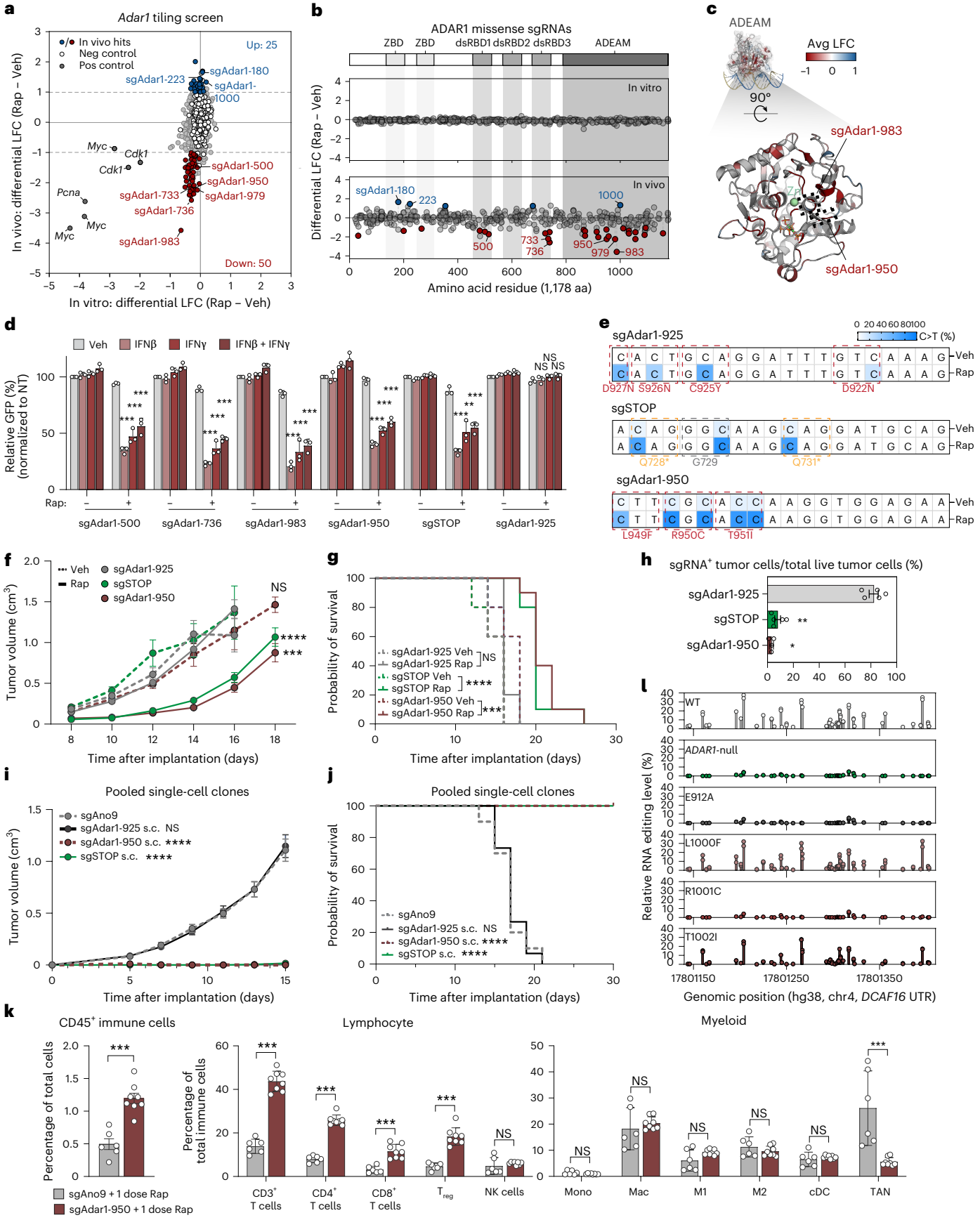

most depleted sgRNAs, were predicted to introduce mutations near the catalytic site (Fig. 5c and Supplementary Fig. 24c), and on-target sequencing confirmed the expected mutations (Fig. 5e and Supplementary Fig. 24d). Notably, these mutations lie near pathogenic variants identified in individuals with dyschromatosis symmetrica hereditaria (M1034I) and Aicardi–Goutières syndrome (K999H)[78,84], linking our screening hits to clinically relevant variants.

Validation and characterization of critical ADAR1 residues

We next sought to validate and characterize top ADAR hits. Because ADAR1 prevents aberrant IFN activation by editing endogenous dsRNAs, IFN-mediated killing provides a functional readout for ADAR1 mutants. We selected four strongly depleted missense sgRNAs (sgAdar1-500, sgAdar1-736, sgAdar1-950 and sgAdar1-983), one nonsense sgRNA (sgSTOP) and a minimally depleted missense control sgRNA (sgAdar1-925) for in vitro testing. Cells edited with loss-of-function sgRNAs exhibited pronounced growth inhibition following IFNβ, IFNγ or their combination treatment (Fig. 5d). Focusing on sgAdar1-950, sgAdar1-925 and sgSTOP for further characterization, immunoblotting showed that sgSTOP substantially reduced ADAR1 levels, whereas sgAdar1-925 had minimal effect, and sgAdar1-950 decreased protein levels by about 40%, suggesting partial destabilization (Supplementary Fig. 24e).

Tumor cells transduced with individual sgRNAs were transplanted into mice and treated with vehicle or a single Rap dose. sgAdar1-925-transduced tumors displayed similar growth and survival under both conditions (Fig. 5f,g), confirming minimal impact of Rap alone on tumor growth and immunity in vivo. By contrast, both sgAdar1-950 and sgSTOP similarly slowed tumor growth and extended survival, suggesting that sgAdar1-950 perturbed residues critical for ADAR1, akin to a functional-null allele (Fig. 5f,g). Flow cytometry analysis showed an ~20-fold depletion of sgAdar1-950- or sgSTOP-edited cells compared to sgAdar1-925 in Rap-treated tumors, consistent with strong negative selection (Fig. 5h).

To validate independently of Rap and to ensure complete base editing, we also generated clonal lines for sgAdar1-925, sgAdar1-950 or sgSTOP, verifying ~100% on-target editing before xenografting (Supplementary Fig. 27a). In vitro, quantitative real-time PCR analysis showed robust induction of IFN-stimulated genes following IFNβ treatment in sgAdar1-950-edited cells, (Supplementary Fig. 27b), whereas in vivo sgAdar1-950-edited tumors exhibited profoundly impaired growth with 100% survival, both phenocopying the sgSTOP-mediated complete *Adar1* knockout (Fig. 5i,j). Immune profiling comparing sgAdar1-950-edited tumors to controls revealed significantly increased $CD45^+$ immune infiltration, including elevated frequencies of $CD3^+$, $CD4^+$, $CD8^+$ and regulatory T cells and reduced tumor-associated neutrophils (Fig. 5k), resembling those reported in *Adar1*-null tumors[6]. By contrast, sgAdar1-925-edited tumors displayed immune profiles similar to unedited controls (Supplementary Fig. 28a,b). Together, these results confirmed that a single dose of Rap had minimal impact on tumor growth and immunity in vivo and that sgAdar1-950 induces a potent loss-of-function phenotype that alters tumor–immune interactions and drives enhanced antitumor immunity.

We next aimed to dissect residue-specific contributions associated with sgAdar1-950. sgAdar1-950 reduced ADAR1 protein by 40% yet phenocopied complete *Adar1* knockout, suggesting that the induced mutation cluster (L949F/R950C/T951I) confers a loss-of-function effect. We therefore introduced the individual corresponding human variants (L1000F, R1001C and T1002I) into *ADAR1*-null HEK293T cells alongside wild-type and deaminase-dead E912A controls. Immunoblotting showed that R1001C and T1002I were expressed comparably to wild-type, whereas L1000F reduced protein stability, consistent with decreased ADAR1 abundance observed with sgAdar1-950 (Supplementary Fig. 29a). Using PKR T446 phosphorylation as a readout, we found that R1001C, but not L1000F, T1002I or wild-type, failed to suppress PKR activation following IFNβ stimulation (Supplementary Fig. 29a). Nanopore long-read sequencing of ADAR1-dependent dsRNA editing sites (3′ UTRs of *DCAF16* and *VPS41*) showed reduced editing by all mutants, with R1001C nearly abolishing activity and phenocopying the deaminase-dead mutant and ADAR1-null cells, consistent with structural analysis showing direct dsRNA contact with R1001 (Fig. 5l and Supplementary Fig. 29b,c). Together, these findings indicate that the L949F/R950C/T951I mutations collectively disrupt both ADAR1 stability and activity, with R950C (human R1001C) acting as the major driver by impairing both PKR suppression and dsRNA editing.

The in vivo screen also identified enriched missense sgRNAs, with the top candidate being sgAdar1-1000, which introduced an A1000T substitution, suggesting a potential gain-of-function effect (Fig. 5a,b). Using a GluA2–GFP reporter line in which ADAR editing restores GFP expression[85], A1000T (human A1051T) increased editing efficiency by ~10% relative to wild-type (Supplementary Fig. 30a). To evaluate in an endogenous context, we generated B16 clones carrying the A1000T edit. Sequencing confirmed ~50% allelic editing, immunoblotting revealed a modest (~10%) increase in ADAR1 protein abundance, and IFNβ-mediated killing assays showed ~10% greater resistance in A1000T-edited clones (Supplementary Fig. 30b–d). AlphaFold3 structural modeling placed A1000 adjacent to an inositol hexakisphosphate binding pocket, implicated in stabilizing ADAR folding, suggesting that A1000T may enhance protein stability and catalytic activity[86,87] (Supplementary Fig. 31). Collectively, these results demonstrate the power of the seBE system for in vivo functional genomics and its utility in identifying and dissecting critical residues of cancer therapeutic targets.

Discussion

Functional genomics enables the discovery of critical cancer dependencies and offers mechanistic insights to inform therapeutic development. Although in vitro functional genetic screens have identified many cell-autonomous dependencies[88], they are limited in revealing non-cell-autonomous dependencies, which involve the interactions between tumors and their physical environment. Traditional BEs with an intact deaminase suffer from nonspecific toxicity, low gene editing efficiency and lack of inducibility, restricting their application for in vivo functional genomics. To bridge this gap, we developed a small-molecule-controlled seBE system enabling rapid and tunable post-translational activation with reduced nonspecific toxicity[45]. Although prior doxycycline-based BEs have shown inducible editing to probe cancer-associated mutants in tumor initiation and progression[44], we demonstrated the utility of seBEs for in vivo functional genetic interrogation of cancer therapeutic vulnerabilities. A single Rap dose could produce highly efficient editing with enhanced phenotypic dynamic range, achieving up to 50% editing efficiency within 1 h of treatment and allowing dose-dependent control (Supplementary Figs. 5 and 6). With this added dimension of temporal control, seBEs are positioned as a powerful system for mapping critical residues across tumor initiation, maintenance, progression and metastasis.

To streamline in vivo screening, we also developed the LASER pipeline for compact sgRNA library design, enriching for highly effective missense sgRNAs. Guided by LASER, we performed in vivo seBE screening across 35 cancer immunity genes and identified clusters of enriched and depleted residues in both positive and negative regulators, reflecting context-dependent functional diversity (Fig. 4c–e). We anticipate that such library compaction should allow larger-scale in vivo genetic screens with reduced animal use or facilitate functional genetic screening using sources with limited primary materials, such as samples from healthy donors or patients.

Through in vitro and in vivo seBE tiling screens, we identified known and uncharacterized critical residues in key cancer dependencies. Epigenetic regulators, including *Arid1a*, *Arid2*, *Ep300* and *Pbrm1*, have been implicated in cancer immunity[9,70,73], yet their large coding sequences limit traditional cDNA-based domain dissection. Of note,

our in vivo seBE screen revealed unexpected context-specific functional phenotypes of individual residues that are missed by total gene knockout (Fig. 4e). For example, despite the high structural similarity of PBRM1's six BDs[89], sgRNAs targeting BD2 and BD5 produced opposite in vivo phenotypes. High-resolution seBE tiling of *Adar1* identified a potent loss-of-function allele R950C and a gain-of-function variant A1000T. The screen also showed that, although all three dsRBDs bind dsRNA, dsRBD1 and dsRBD3 play dominant roles in modulating tumor immune signaling with specific residues now nominated as potential therapeutic targets. Collectively, our findings demonstrate the versatility and modularity of the seBE system, which offers controllable and robust genome editing capabilities as a means to systematically identify critical residues for cancer functional genomics.

Online content

Any methods, additional references, Nature Portfolio reporting summaries, source data, extended data, supplementary information, acknowledgements, peer review information; details of author contributions and competing interests; and statements of data and code availability are available at https://doi.org/10.1038/s41587-026-03077-5.

References

1. Chow, R. D. & Chen, S. Cancer CRISPR screens in vivo. *Trends Cancer* **4**, 349–358 (2018).
2. Haley, B. & Roudnicky, F. Functional genomics for cancer drug target discovery. *Cancer Cell* **38**, 31–43 (2020).
3. Li, C. & Kasinski, A. L. In vivo cancer-based functional genomics. *Trends Cancer* **6**, 1002–1017 (2020).
4. Przybyla, L. & Gilbert, L. A. A new era in functional genomics screens. *Nat. Rev. Genet.* **23**, 89–103 (2022).
5. Manguso, R. T. et al. In vivo CRISPR screening identifies *Ptpn2* as a cancer immunotherapy target. *Nature* **547**, 413–418 (2017).
6. Ishizuka, J. J. et al. Loss of ADAR1 in tumours overcomes resistance to immune checkpoint blockade. *Nature* **565**, 43–48 (2019).
7. Dubrot, J. et al. In vivo screens using a selective CRISPR antigen removal lentiviral vector system reveal immune dependencies in renal cell carcinoma. *Immunity* **54**, 571–585 (2021).
8. Dubrot, J. et al. In vivo CRISPR screens reveal the landscape of immune evasion pathways across cancer. *Nat. Immunol.* **23**, 1495–1506 (2022).
9. Griffin, G. K. et al. Epigenetic silencing by SETDB1 suppresses tumour intrinsic immunogenicity. *Nature* **595**, 309–314 (2021).
10. Wang, X. et al. In vivo CRISPR screens identify the E3 ligase COP1 as a modulator of macrophage infiltration and cancer immunotherapy target. *Cell* **184**, 5357–5374 (2021).
11. Shalem, O. et al. Genome-scale CRISPR–Cas9 knockout screening in human cells. *Science* **343**, 84–87 (2014).
12. Wang, T., Wei, J. J., Sabatini, D. M. & Lander, E. S. Genetic screens in human cells using the CRISPR–Cas9 system. *Science* **343**, 80–84 (2014).
13. Shi, J. et al. Discovery of cancer drug targets by CRISPR–Cas9 screening of protein domains. *Nat. Biotechnol.* **33**, 661–667 (2015).
14. Grevet, J. D. et al. Domain-focused CRISPR screen identifies HRI as a fetal hemoglobin regulator in human erythroid cells. *Science* **361**, 285–290 (2018).
15. Cao, Z. et al. ZMYND8-regulated IRF8 transcription axis is an acute myeloid leukemia dependency. *Mol. Cell* **81**, 3604–3622 (2021).
16. Tarumoto, Y. et al. LKB1, salt-inducible kinases, and MEF2C are linked dependencies in acute myeloid leukemia. *Mol. Cell* **69**, 1017–1027 (2018).
17. Lu, B. et al. A transcription factor addiction in leukemia imposed by the MLL promoter sequence. *Cancer Cell* **34**, 970–981 (2018).
18. Komor, A. C., Kim, Y. B., Packer, M. S., Zuris, J. A. & Liu, D. R. Programmable editing of a target base in genomic DNA without double-stranded DNA cleavage. *Nature* **533**, 420–424 (2016).
19. Gaudelli, N. M. et al. Programmable base editing of A*T to G*C in genomic DNA without DNA cleavage. *Nature* **551**, 464–471 (2017).
20. Koblan, L. W. et al. Improving cytidine and adenine base editors by expression optimization and ancestral reconstruction. *Nat. Biotechnol.* **36**, 843–846 (2018).
21. Thuronyi, B. W. et al. Continuous evolution of base editors with expanded target compatibility and improved activity. *Nat. Biotechnol.* **37**, 1070–1079 (2019).
22. Richter, M. F. et al. Phage-assisted evolution of an adenine base editor with improved Cas domain compatibility and activity. *Nat. Biotechnol.* **38**, 883–891 (2020).
23. Xiao, Y. L., Wu, Y. & Tang, W. An adenine base editor variant expands context compatibility. *Nat. Biotechnol.* **42**, 1442–1453 (2024).
24. Cuella-Martin, R. et al. Functional interrogation of DNA damage response variants with base editing screens. *Cell* **184**, 1081–1097 (2021).
25. Hanna, R. E. et al. Massively parallel assessment of human variants with base editor screens. *Cell* **184**, 1064–1080 (2021).
26. Xu, P. et al. Genome-wide interrogation of gene functions through base editor screens empowered by barcoded sgRNAs. *Nat. Biotechnol.* **39**, 1403–1413 (2021).
27. Sangree, A. K. et al. Benchmarking of SpCas9 variants enables deeper base editor screens of BRCA1 and BCL2. *Nat. Commun.* **13**, 1318 (2022).
28. Coelho, M. A. et al. Base editing screens map mutations affecting interferon-γ signaling in cancer. *Cancer Cell* **41**, 288–303 (2023).
29. Lue, N. Z. et al. Base editor scanning charts the DNMT3A activity landscape. *Nat. Chem. Biol.* **19**, 176–186 (2023).
30. Martin-Rufino, J. D. et al. Massively parallel base editing to map variant effects in human hematopoiesis. *Cell* **186**, 2456–2474 (2023).
31. Perner, F. et al. *MEN1* mutations mediate clinical resistance to menin inhibition. *Nature* **615**, 913–919 (2023).
32. Schmidt, R. et al. Base-editing mutagenesis maps alleles to tune human T cell functions. *Nature* **625**, 805–812 (2024).
33. Li, Y. et al. Functional profiling of serine, threonine and tyrosine sites. *Nat. Chem. Biol.* **21**, 532–543 (2025).
34. Li, H. et al. Assigning functionality to cysteines by base editing of cancer dependency genes. *Nat. Chem. Biol.* **19**, 1320–1330 (2023).
35. Sanchez-Rivera, F. J. et al. Base editing sensor libraries for high-throughput engineering and functional analysis of cancer-associated single nucleotide variants. *Nat. Biotechnol.* **40**, 862–873 (2022).
36. Kim, Y. et al. High-throughput functional evaluation of human cancer-associated mutations using base editors. *Nat. Biotechnol.* **40**, 874–884 (2022).
37. Coelho, M. A. et al. Base editing screens define the genetic landscape of cancer drug resistance mechanisms. *Nat. Genet.* **56**, 2479–2492 (2024).
38. Walsh, Z. H. et al. Mapping variant effects on anti-tumor hallmarks of primary human T cells with base-editing screens. *Nat. Biotechnol.* **43**, 384–395 (2025).
39. Grunewald, J. et al. Transcriptome-wide off-target RNA editing induced by CRISPR-guided DNA base editors. *Nature* **569**, 433–437 (2019).
40. Grunewald, J. et al. CRISPR DNA base editors with reduced RNA off-target and self-editing activities. *Nat. Biotechnol.* **37**, 1041–1048 (2019).
41. Jin, S. et al. Cytosine, but not adenine, base editors induce genome-wide off-target mutations in rice. *Science* **364**, 292–295 (2019).

42. Zuo, E. et al. Cytosine base editor generates substantial off-target single-nucleotide variants in mouse embryos. *Science* **364**, 289–292 (2019).
43. Fiumara, M. et al. Genotoxic effects of base and prime editing in human hematopoietic stem cells. *Nat. Biotechnol.* **42**, 877–891 (2024).
44. Katti, A. et al. Generation of precision preclinical cancer models using regulated in vivo base editing. *Nat. Biotechnol.* **42**, 437–447 (2024).
45. Berrios, K. N. et al. Controllable genome editing with split-engineered base editors. *Nat. Chem. Biol.* **17**, 1262–1270 (2021).
46. Zuber, J. et al. Mouse models of human AML accurately predict chemotherapy response. *Genes Dev.* **23**, 877–889 (2009).
47. Gier, R. A. et al. High-performance CRISPR–Cas12a genome editing for combinatorial genetic screening. *Nat. Commun.* **11**, 3455 (2020).
48. Burnett, P. E., Barrow, R. K., Cohen, N. A., Snyder, S. H. & Sabatini, D. M. RAFT1 phosphorylation of the translational regulators p70 S6 kinase and 4E-BP1. *Proc. Natl Acad. Sci. USA* **95**, 1432–1437 (1998).
49. Pattabiraman, D. R. & Gonda, T. J. Role and potential for therapeutic targeting of MYB in leukemia. *Leukemia* **27**, 269–277 (2013).
50. Vollmuth, F., Blankenfeldt, W. & Geyer, M. Structures of the dual bromodomains of the P-TEFb-activating protein BRD4 at atomic resolution. *J. Biol. Chem.* **284**, 36547–36556 (2009).
51. Filippakopoulos, P. et al. Selective inhibition of BET bromodomains. *Nature* **468**, 1067–1073 (2010).
52. Dawson, M. A. et al. Inhibition of BET recruitment to chromatin as an effective treatment for MLL-fusion leukaemia. *Nature* **478**, 529–533 (2011).
53. Shi, J. et al. Role of SWI/SNF in acute leukemia maintenance and enhancer-mediated Myc regulation. *Genes Dev.* **27**, 2648–2662 (2013).
54. Inoue, T., Heo, W. D., Grimley, J. S., Wandless, T. J. & Meyer, T. An inducible translocation strategy to rapidly activate and inhibit small GTPase signaling pathways. *Nat. Methods* **2**, 415–418 (2005).
55. Edwards, S. R. & Wandless, T. J. The rapamycin-binding domain of the protein kinase mammalian target of rapamycin is a destabilizing domain. *J. Biol. Chem.* **282**, 13395–13401 (2007).
56. Liang, F. S., Ho, W. Q. & Crabtree, G. R. Engineering the ABA plant stress pathway for regulation of induced proximity. *Sci. Signal.* **4**, rs2 (2011).
57. Walton, R. T., Christie, K. A., Whittaker, M. N. & Kleinstiver, B. P. Unconstrained genome targeting with near-PAMless engineered CRISPR–Cas9 variants. *Science* **368**, 290–296 (2020).
58. Gajula, K. S. et al. High-throughput mutagenesis reveals functional determinants for DNA targeting by activation-induced deaminase. *Nucleic Acids Res.* **42**, 9964–9975 (2014).
59. Gehrke, J. M. et al. An APOBEC3A–Cas9 base editor with minimized bystander and off-target activities. *Nat. Biotechnol.* **36**, 977–982 (2018).
60. Berrios, K. N. et al. Cooperativity between Cas9 and hyperactive AID establishes broad and diversifying mutational footprints in base editors. *Nucleic Acids Res.* **52**, 2078–2090 (2024).
61. Arbab, M. et al. Determinants of base editing outcomes from target library analysis and machine learning. *Cell* **182**, 463–480 (2020).
62. Goldenberg, O., Erez, E., Nimrod, G. & Ben-Tal, N. The ConSurf-DB: pre-calculated evolutionary conservation profiles of protein structures. *Nucleic Acids Res.* **37**, D323–D327 (2009).
63. Laine, E., Karami, Y. & Carbone, A. GEMME: a simple and fast global epistatic model predicting mutational effects. *Mol. Biol. Evol.* **36**, 2604–2619 (2019).
64. Ben Chorin, A. et al. ConSurf-DB: an accessible repository for the evolutionary conservation patterns of the majority of PDB proteins. *Protein Sci.* **29**, 258–267 (2020).
65. Notin, P. et al. TranceptEVE: combining family-specific and family-agnostic models of protein sequences for improved fitness prediction. Preprint at *bioRxiv* https://doi.org/10.1101/2022.12.07.519495 (2022).
66. Lin, Z. et al. Evolutionary-scale prediction of atomic-level protein structure with a language model. *Science* **379**, 1123–1130 (2023).
67. Notin, P. et al. Proteingym: large-scale benchmarks for protein fitness prediction and design. *Adv. Neur. Inf. Process. Syst.* **36**, 64331–64379 (2023).
68. Qiu, J. et al. Cancer cells resistant to immune checkpoint blockade acquire interferon-associated epigenetic memory to sustain T cell dysfunction. *Nat. Cancer* **4**, 43–61 (2023).
69. Benci, J. L. et al. Tumor interferon signaling regulates a multigenic resistance program to immune checkpoint blockade. *Cell* **167**, 1540–1554 (2016).
70. Pan, D. et al. A major chromatin regulator determines resistance of tumor cells to T cell-mediated killing. *Science* **359**, 770–775 (2018).
71. Lawson, K. A. et al. Functional genomic landscape of cancer-intrinsic evasion of killing by T cells. *Nature* **586**, 120–126 (2020).
72. Mathew, D. et al. Combined JAK inhibition and PD-1 immunotherapy for non-small cell lung cancer patients. *Science* **384**, eadf1329 (2024).
73. Maxwell, M. B. et al. ARID1A suppresses R-loop-mediated STING-type I interferon pathway activation of anti-tumor immunity. *Cell* **187**, 3390–3408 (2024).
74. Liddicoat, B. J. et al. RNA editing by ADAR1 prevents MDA5 sensing of endogenous dsRNA as nonself. *Science* **349**, 1115–1120 (2015).
75. Pestal, K. et al. Isoforms of RNA-editing enzyme ADAR1 independently control nucleic acid sensor MDA5-driven autoimmunity and multi-organ development. *Immunity* **43**, 933–944 (2015).
76. Samuel, C. E. Adenosine deaminase acting on RNA (ADAR1), a suppressor of double-stranded RNA-triggered innate immune responses. *J. Biol. Chem.* **294**, 1710–1720 (2019).
77. Li, Q. et al. RNA editing underlies genetic risk of common inflammatory diseases. *Nature* **608**, 569–577 (2022).
78. Rice, G. I. et al. Mutations in ADAR1 cause Aicardi–Goutieres syndrome associated with a type I interferon signature. *Nat. Genet.* **44**, 1243–1248 (2012).
79. Hayashi, M. & Suzuki, T. Dyschromatosis symmetrica hereditaria. *J. Dermatol.* **40**, 336–343 (2013).
80. Mannion, N. M. et al. The RNA-editing enzyme ADAR1 controls innate immune responses to RNA. *Cell Rep.* **9**, 1482–1494 (2014).
81. Rice, G. I. et al. Gain-of-function mutations in *IFIH1* cause a spectrum of human disease phenotypes associated with upregulated type I interferon signaling. *Nat. Genet.* **46**, 503–509 (2014).
82. de Reuver, R. & Maelfait, J. Novel insights into double-stranded RNA-mediated immunopathology. *Nat. Rev. Immunol.* **24**, 235–249 (2024).
83. Park, S. et al. High-throughput mutagenesis reveals unique structural features of human ADAR1. *Nat. Commun.* **11**, 5130 (2020).
84. Kono, M., Akiyama, M., Suganuma, M., Tomita, Y. & Sanchez-Valle, A. Dyschromatosis symmetrica hereditaria by ADAR1 mutations and viral encephalitis: a hidden link? *Int. J. Dermatol.* **52**, 1582–1584 (2013).
85. Fritzell, K., Xu, L. D., Otrocka, M., Andreasson, C. & Ohman, M. Sensitive ADAR editing reporter in cancer cells enables high-throughput screening of small molecule libraries. *Nucleic Acids Res.* **47**, e22 (2019).

86. Macbeth, M. R. et al. Inositol hexakisphosphate is bound in the ADAR2 core and required for RNA editing. *Science* **309**, 1534–1539 (2005).
87. Deng, X. et al. Biochemical profiling and structural basis of ADAR1-mediated RNA editing. *Mol. Cell* **85**, 1381–1394 (2025).
88. Arafeh, R., Shibue, T., Dempster, J. M., Hahn, W. C. & Vazquez, F. The present and future of the Cancer Dependency Map. *Nat. Rev. Cancer* **25**, 59–73 (2025).
89. Filippakopoulos, P. & Knapp, S. Targeting bromodomains: epigenetic readers of lysine acetylation. *Nat. Rev. Drug Discov.* **13**, 337–356 (2014).

Methods

Cell lines and culture

The mouse RN2 acute myeloid leukemia cell line was grown in RPMI-1640 (Gibco) with 10% fetal bovine serum (FBS). The human K562 chronic myeloid leukemia cell line was grown in RPMI-1640 with 10% bovine calf serum. The mouse B16-F10 melanoma cell line was grown in DMEM (Corning) with 10% FBS. The HEK293T cell line was cultured in DMEM with 10% bovine calf serum. All cell culture media were supplemented with 1% penicillin/streptomycin. Cells were cultured at 37 °C with 5% CO_2 and periodically tested to be mycoplasma negative.

Vector construction and sgRNA cloning

PCR fragments were amplified with Phusion High-Fidelity DNA Polymerase (Thermo Scientific). Vectors were generated using the In-Fusion HD Cloning system (Takara Bio). The intact BE was cloned from Lenti-evoA1-BE4max (Addgene, 174700). The SpCas9 expression vector is Addgene 108100. For seBE-evoA1, the C-terminal ($seBE_C$) construct corresponds to Addgene 174702, and the N-terminal ($seBE_N$) construct corresponds to Addgene 174701, with mCherry–P2A-Neo replaced with a GFP mark. seBE-A3A was cloned from Addgene 174698, and split-AID* was cloned from Addgene 174697. The SpG nickase was generated from Addgene 139998 and subcloned into the $seBE_C$ vector. For sgRNA cloning, cDNA oligonucleotides were annealed and phosphorylated with T4 polynucleotide kinase (New England Biolabs) and ligated into BsmBI-digested $seBE_N$ vector or LRG2.1T (Addgene, 108098). ABI-PYL1 heterodimerization domains were cloned from Addgene 38247 into seBE vectors. Lenti-A3Ac-puro and Lenti-A3An-LRG2.1T used for in vivo base editing have been deposited at Addgene (253342 and 253343).

Lentiviral production and transduction

For cancer cell experiments, HEK293T cells were seeded at ~50% confluency in 10-cm plates 1 day ahead and transfected at ~90% confluency. For each viral production, 10 µg of the plasmid of interest, 5 µg of vesicular stomatitis virus glycoprotein and 7.5 µg of psPAX2 (Addgene, 12260) were transfected using 80 µl of polyethylenimine (Polysciences, PEI 25000) in 500 µl of OPTI-MEM (Gibco). Media were replaced with ~6 ml of fresh DMEM 6–8 h after transfection. Lentivirus was collected several times within 48 h after transfection and filtered with a 0.45-µm PVDF filter (Millipore).

For primary T cells, HEK293T cells were seeded on 15-cm poly-D-lysine-coated plates (Corning) and maintained overnight in 20 ml of complete OPTI-MEM (Gibco), consisting of GlutaMAX (Gibco) supplemented with 5% FBS, 1 mM sodium pyruvate (Fisher Scientific) and 1× MEM nonessential amino acids (Fisher Scientific). Transfection was performed by mixing a 1.5-ml solution of OPTI-MEM with 110 µl of Lipofectamine 3000 reagent (Fisher Scientific, L3000075) with a second 1.5-ml solution of OPTI-MEM with 27 µg of the plasmid of interest, 19 µg of psPAX2, 8.4 µg of pMD2.G and 100 µl of P3000 reagent. After a 20-min incubation at room temperature, transfection complexes were added dropwise. Twenty milliliters of fresh complete OPTI-MEM supplemented with 1× ViralBoost (Alstem, VB100) was added to the plate 6 h after transfection. Lentivirus was collected and concentrated 100-fold with LentiX Concentrator (Takara, 631231) 18 h after transfection.

Cells were transduced with lentivirus using 8 µg ml^{-1} Polybrene (Sigma, H9268), centrifuged at 650*g* for 25 min at room temperature, incubated at 37 °C overnight and replaced with fresh medium ~15 h after transduction. Antibiotics were added 1 day after infection at appropriate concentrations (10 µg ml^{-1} blasticidin, 2 µg ml^{-1} puromycin).

Competition-based cellular proliferation assay

Cells stably expressing either the intact BE or the seBE were lentivirally transduced with the indicated sgRNAs coexpressed with a GFP reporter. Transductions were performed at a low MOI (<0.5) to ensure single-copy integration. The percentage of GFP^+sgRNA^+ cells was measured on day 3 after infection using either a Guava Easycyte HT instrument (Millipore) or a CytoFLEX Flow Cytometer (Beckman). For seBE experiments, Rap (LC Laboratories, R-5000), rapalog (A/C Heterodimerizer, Takara, 635057), abscisic acid (Millipore, 5.30339) or vehicle was added at day 3 after infection and replenished at each cell passage. The LFC in the GFP^+ population relative to baseline was used for analysis.

GFP disruption assay

Stable K562 and HEK293T cell lines expressing a d2GFP reporter were established[47]. For K562 d2GFP experiments, cells were transduced with wild-type or FRB-mutated seBE constructs. sgRNAs targeting GFP to introduce a premature stop codon were coexpressed with mCherry. Rap or the rapalog was added starting on day 0. The fold change of GFP^+ cells in the $mCherry^+$ population was analyzed on day 8. For HEK293T d2GFP experiments, cells were transfected with ABI-PYL1-based or Rap-inducible seBE vectors together with GFP-targeting sgRNA. Transfections were performed using 50 µl of jetPRIME buffer, 2.4 µl of jetPRIME reagent (Polyplus) and 0.6 µg of plasmid DNA. Media were replaced after 4 h, and abscisic acid or Rap was added accordingly. The fold change of GFP^+ cells in the $mCherry^+$ population was analyzed on day 3 after transfection.

Immunoblotting

Cells were lysed using a 25-mm syringe in Laemmli sample buffer (Bio-Rad) containing 5% β-mercaptoethanol. Protein extracts were denatured at 95 °C for 7 min and loaded onto SDS polyacrylamide gels. Proteins were transferred to 0.45-µm nitrocellulose membranes, blocked with 5% milk in TBST buffer (Tris-buffered saline with Tween 20) at room temperature for 30 min and incubated overnight at 4 °C with primary antibodies in 5% milk/TBST with shaking. After three 5-min washes in PBST buffer (phosphate-buffered saline with Tween 20), membranes were incubated with secondary antibodies in 1× blocking buffer (LI-COR) at room temperature for 45 min. Membranes were washed again three times as described earlier, and imaging was performed using an Odyssey CLx (LI-COR) imager. Quantification was conducted using ImageStudio Lite or ImageJ (version 1.54g). The antibodies used are listed in Supplementary Table 8.

RNA-seq and data analysis

RN2 cells transduced with nCas9, intact BE-evoA1, intact BE with catalytic mutation of the DNA deaminase (evoA1) or seBE-evoA1 constructs were sorted on day 5 after transduction. RN2 intact BE and seBE cells were treated with 1 nM Rap or vehicle 24 h before sorting. Samples were prepared with three independent biological replicates. Total RNA was extracted from about 1 million cells using a Direct-zol RNA Miniprep Plus kit (Zymo) with DNase I treatment. RNA-seq libraries were prepared and sequenced by Novogene using 2 × 150 bp paired-end reads with 6 GB raw data per sample.

For RNA-seq analysis, raw FASTQ files were filtered and adapter trimmed with fastp (v1.0.1)[90] using the following parameters: --trim_tail1 5 --trim_tail2 5 --detect_adapter_for_pe --length_required 100. Trimmed reads were aligned to the mouse reference genome (GRCm39) using STAR (v2.7.1a) in two-pass mode[91] (--twopassMode Basic). Alignments used --outFilterMismatchNmax 5 and --outFilterMultimapNmax 10 and were written as coordinate-sorted BAM with tags (NH HI AS nM MD NM XS) and MAPQ 60 for unique alignments (--outSAMmapqUnique 60). STAR was run with --quantMode GeneCounts TranscriptomeSAM to generate per-gene counts and transcriptome-mapped reads. BAM files were indexed with samtools (v1.9)[92]. Primary gene-level quantification was performed with featureCounts[93] (Subread v2.0.3) using -t exon -g gene_id -p --countReadPairs -B -Q 20 -s 2 (reverse stranded) against the matched composite GTF. Count matrices were imported to R, and differential expression was performed with DESeq2 (ref. 94). Genes with an | LFC | of greater than 0.5 and an adjusted *P* value of less than 0.05

were considered significantly up- or downregulated. Variant calling was performed according to the iBE pipeline[44].

On-target sequencing

Genomic DNA was isolated using a Quick-DNA Miniprep kit (Zymo Research). A total of 150 ng of genomic DNA was used as input to amplify the locus of interest and attach common sequencing overhangs. Purified PCR products were sent for Amplicon sequencing (Azenta) or sequenced in-house on an Illumina MiSeq platform. Data were processed using EditR[95] or CRISPResso2 (ref. 96). Primers are provided in Supplementary Table 9.

BE tiling library design and cloning

The sgRNA libraries include all possible sgRNAs with NGG or NG PAM sequences targeting the UTRs, exons and flanking intronic regions of *Myb* (ENSMUST00000020158), *Brd4* (ENSMUST00000121285), *Smarca4* (ENSMUST00000174008) and *Adar1* (ENSMUSG00000027951), excluding sgRNAs with multiple genome mappings, BsmBI sites or TTTT sequences. Negative controls (which target nonessential genes and were specifically chosen to contain at least one editable cytosine within the optimal editing window) and positive controls (essential genes or established leukemia dependencies) were included. Pooled sgRNAs were synthesized (Twist Bioscience) and cloned into BsmBI-digested LRG2.1T or LRG2.1T-seBE$_N$ vectors using the Gibson assembly method (New England Biolabs).

All possible sgRNAs of *Myb*, *Brd4* and *Smarca4* were annotated based on the targeted cytosine in positions 1–9 for seBE-evoA1 and positions 1–15 for seBE-A3A and comparisons of other BE systems. sgRNAs with no cytosine in the editing window were classified as 'no edit'. The remaining sgRNAs were categorized based on their potential target region and editing outcomes, including 'UTR', 'intron', 'silent', 'missense', 'nonsense' and 'splicing site'. 'Nonsense' and 'splicing site' sgRNAs were considered more severe than 'missense' sgRNAs, which were considered more severe than the other categories. sgRNAs that resulted in multiple mutation types were classified according to the most severe mutation.

Pooled screenings in vitro

Cells were transduced in two biological replicates with the lentiviral library. Viral titration achieved an MOI of ~0.3–0.5 to ensure single-copy integration. On day 3 after infection, cells were collected at 1,000× sgRNA coverage of the pooled library. Rap (1 nM) or vehicle was then added. On day 12 after treatment, cells were collected again at 1,000× sgRNA coverage. Collected cells were washed with PBS, pelleted and stored at −80 °C until genomic DNA extraction. Genomic DNA was isolated, and sgRNA cassette quantification was performed via deep sequencing[47].

BE screening analysis

Each sgRNA was sequenced to a depth of approximately 1,000× coverage. Sequencing data were demultiplexed into fastq files and analyzed using MAGeCK[97]. sgRNAs with less than 100× coverage of the initial time point were excluded from further analysis. A MAGeCK test was performed to calculate LFC values and the *P* values of sgRNAs across two independent biological replicates, comparing different time points relative to the null distribution of negative controls. The initial time point was used as MAGeCK control input, and the final time point was used as the treatment input. The fold change of an sgRNA was capped at a maximum of 100.

Recombinant protein expression and purification

Wild-type and mutant versions of MYB DBD (UniProt ID: P10242-1, residues 35–193) were cloned into the pET28a backbone with a 6×His–ECFP tag at the N terminus. BL21-CodonPlus (DE3)-RIPL (Agilent) competent bacteria were transformed with the expression plasmids. Large-scale liquid cultures were induced at 30 °C with 0.5 mM IPTG for 3 h. Bacteria were collected by centrifugation, and recombinant proteins were extracted using lysis buffer (50 mM Tris-phosphate pH 7.5, 500 mM NaCl, 10% glycerol, 20 mM imidazole, 0.2 mM phenylmethanesulfonyl fluoride, 1:100 protease inhibitor cocktail and 1 mM DTT). The lysates were incubated with 0.5 mg ml^{-1} lysozyme on ice and sonicated. The crude lysate was clarified by centrifugation using a Fiberlite F21-8 × 50y Fixed-Angle Rotor (Thermo) at 38,000*g* at 4 °C for 1 h. The recombinant proteins were affinity purified using Ni-NTA slurry (Qiagen) and washed extensively with lysis buffer and then wash buffer (50 mM Tris pH 7.5, 150 mM NaCl and 10% glycerol). Finally, bound proteins were eluted in elution buffer (50 mM Tris pH 7.5, 150 mM NaCl and 250 mM midazole), and 2 mM EDTA and 1 mM DTT were added immediately to the eluted proteins. The proteins were further purified through Superdex 75 increase columns (Cytiva) using 50 mM sodium phosphate pH 7.5, 100 mM NaCl and 1 mM EDTA as running buffer. The fractions were run on an SDS–PAGE gel to check the purity and pooled. Protein concentration was determined using a Nanodrop.

Electrophoretic mobility shift assay

Top and bottom oligonucleotides for the 2× MRE probe[98] were synthesized by Sigma. Single-stranded DNA oligonucleotides were mixed in an equimolar ratio in oligonucleotide annealing buffer (10 mM Tris pH 8.0 and 50 mM NaCl), boiled for 5 min at 95 °C and allowed to cool down to room temperature. Duplex DNA (20 nM) was then incubated with varying concentrations (0–200 nM) of the MYB DNA-binding domain (MYB DBD wild-type, E99K and D100N) in 20 µl of binding buffer (20 mM Tris pH 8.0, 0.1 mM EDTA, 10% glycerol, 80 mM NaCl, 0.1 mM DTT and 0.01% Brij-35). The DNA–protein mixture was incubated at room temperature for 30 min. After incubation, 6× DNA loading dye (15% Ficoll and 0.9% Orange G) was added to the binding reactions. Half of the mixtures were loaded onto a 6% DNA retardation gel and electrophoresed for 1 h at 100 V and 4 °C using 0.5× TBE running buffer. Gels were stained in 1× SYBR Gold in 0.5× TBE for 20 min at room temperature and visualized using a UV transilluminator.

Flow cytometry

RN2 cells transduced with intact BE or seBE constructs were analyzed on day 5 after transduction using a BD Pharmingen BrdU Flow kit (BD, 552598), with DAPI used for DNA content staining. RN2 intact BE$^+$ and seBE$^+$ cells were treated with 1 nM Rap or vehicle control for 24 h before staining. For in vitro *Cd44* editing, seBE$^+$ sorted B16-F10 cells were treated with or without Rap and stained with anti-CD44 for 30 min at 4 °C. For quantification of tumor immune infiltration, whole tumors were collected, fully dissociated and stained for flow cytometric analysis. Live/dead cell discrimination was performed using a Live/Dead Fixable Aqua Dead Cell Stain kit (Invitrogen, L34966). Total immune cells were identified as CD45$^+$, natural killer cells as NK1.1$^+$CD3$^-$, total T cells as NK1.1$^-$CD3$^+$, regulatory T cells as CD4$^+$FOXP3$^+$, dendritic cells as CD11b$^+$CD11c$^+$MHC class II$^+$, tumor-associated neutrophils as CD11b$^+$Ly6G$^+$Ly6C$^+$, macrophages as F4/80$^+$CD11b$^+$, M1 as F4/80$^+$CD11b$^+$MHC class II$^+$, M2 as F4/80$^+$CD11b$^+$MHC class II$^-$ and monocytes as CD11b$^+$Ly6C$^+$. All flow cytometric analyses were performed using an LSR II (BD) and analyzed with FlowJo software (TreeStar). The antibodies used are listed in Supplementary Table 8.

Pooled screenings in vivo

All animal experiments were conducted in accordance with a protocol (803042) approved by the Institutional Animal Care and Use Committee of the University of Pennsylvania. Five- to 7-week-old female C57BL/6 mice were obtained from Charles River Laboratory, maintained under specific pathogen-free conditions and randomly assigned to experimental groups. On day 0, 5 × 10^5 B16-F10 seBE$^+$ sorted cells were mixed with an equal volume of basement membrane extract (Bio-Techne) and subcutaneously injected into each flank of the mice.

For the *Adar1* seBE tiling screen, two independent biological replicates were performed, with six mice used per treatment group, whereas for the LASER-designed seBE screen, five to ten mice were used per treatment group. Rap was prepared in 5% PEG400 and 5% Tween 80 solution and administered intraperitoneally at a dose of 4 mg per kg (body weight). For the *Adar1* seBE tiling screen, a single Rap dose was administered on day 3 after implantation, whereas for the LASER-designed seBE screen, Rap was administered on days 3 and 6 after implantation. Control groups received an equivalent volume of vehicle. Tumors were collected on day 15 after implantation. Single-cell suspensions were prepared, red blood cells were lysed using ACK Lysis Buffer (Life Technologies), and dead cells were removed using a Dead Cell Removal kit (Miltenyi Biotec). B16-F10 seBE$^+$ cells were collected to ensure at least 1,000× sgRNA coverage, based on percent GFP detection. The collected cells were used for library preparation following the protocol described for in vitro experiments.

In vitro cytokine stimulation and cell growth competition assay

For in vitro validation of *Adar1* sgRNA hits, seBE$_C^+$ B16 cells were transduced with the indicated sgRNAs coexpressed with GFP. Cells were first treated with 1 nM Rap or vehicle for 72 h to induce editing, plated into 24-well plates at ~30,000 cells per well and cultured for an additional 72 h with IFNβ (1,000 U ml^{-1}, PBL), IFNγ (100 ng ml^{-1}, Cell Signaling Technologies) or both. The percentage of GFP$^+$ cells was measured using a CytoFLEX flow cytometer, and growth inhibition was calculated and normalized to vehicle-treated negative-control conditions for each sgRNA.

ADAR1 editing reporter assay

An ADAR1-preferential dsRNA sequence derived from GluA2, containing the canonical R/G editing site, was modified to introduce a premature stop codon (TAG) within the editable region[85]. This GluA2 reporter was cloned in-frame with a d2GFP reporter. Following ADAR1-mediated editing, the stop codon is recoded to tryptophan (TGG), restoring d2GFP expression. HEK293T cells were first lentivirally transduced with the GluA2–d2GFP reporter and transiently transfected with the indicated ADAR1 vectors coexpressing an mCherry to track expression. The proportions of mCherry$^+$ and GFP$^+$ cells were quantified using a CytoFLEX flow cytometer. ADAR1 RNA editing efficiency was calculated as the percentage of GFP$^+$ cells within the mCherry$^+$ population.

Quantitative PCR

RNA was extracted using a NucleoSpin RNA Plus kit (MACHEREY–NAGELTM), and cDNA synthesis was performed using qScript XLT cDNA SuperMix (Quantabio) with 1 µg of RNA. Real-time PCR was performed using Power SYBR Green PCR Master Mix (Applied Biosystems) on a QuantStudio 6 Pro real-time PCR system (Applied Biosystems). Cycling threshold (C_t) values were determined using the QuantStudio desktop analysis software.

ADAR1 variant validation

The plasmid expressing wild-type ADAR1, pDY1173_ADAR1p150, was purchased from Addgene (plasmid 193192), and the plasmids carrying mutant *ADAR1* were generated using a QuickChange II XL Site-Directed Mutagenesis kit (Agilent Technologies). *ADAR1*-knockout HEK293T cells were a gift from B. Li (Stanford University)[99]. The cells were maintained in DMEM (Gibco) supplemented with 10% FBS and penicillin/streptomycin. Transfection was performed with Avalanche-Omni Transfection Reagent (EZ Biosystems), with 80–90% transfection efficiency in general in the presence or absence of IFNβ (239 U ml^{-1}, 11415-1).

For RNA editing analysis, RNA was extracted from 500,000 cells using an RNeasy Mini kit (74104, Qiagen). In total, 0.5–1 µg of RNA was reverse transcribed using Induro Reverse Transcriptase (M0681S, New England Biolabs). PCR was performed using the PrimeSTAR GXL Premix system (R051A, Takara). PCR products were purified using a QIAquick PCR Purification kit (28106, Qiagen). Editing efficiency was assessed using Nanopore sequencing (Azenta).

A human reference editome comprising >2.8 million publicly available RNA editing sites was compiled[77]. FASTQ files were quality controlled using fastp (v1.0.1) with the -t 1 -5 -3 flags. Clean reads were aligned to the human reference genome (GRCh38) using minimap2 (v2.30). Samples were required to have >90% of reads aligned to the target PCR regions and a minimum coverage of >50×. RNA editing sites within the target regions were extracted, and editing levels were quantified using a custom script (https://hub.docker.com/r/vanessa/mpileup/). RNA editing level was defined as G / (A + G), representing the fraction of edited G reads among all A and G reads at each site.

Language models for sgRNA library design

To select sgRNAs that cause missense mutations, each sgRNA was first annotated based on predicted bystander sequences and their associated scores. Using the corresponding BE-Hive model[61], sgRNA genotypes for bystander sequences and their probabilities were predicted; the BE mode was set to evoAPOBEC, eA3A or AID, and the cell type was set to mouse embryonic stem cells. Bystander sequences were annotated to indicate whether they contained nonsense, splicing-altering, missense or nonsignificant mutations, with prioritization in that order (for example, a genotype with both nonsense and missense mutations was annotated as nonsense). A state-of-the-art splicing-effect prediction model, Pangolin[100], was used to assess splicing alterations, additionally annotating those bystander sequences with scores higher than 0.5 as splicing-altering. For each sgRNA, the cumulative probability of each type of annotation was calculated, and the most predominant annotation was assigned at the sgRNA level. If a nonsignificant mutation was the most predominant, any annotation with a cumulative probability greater than 25% was assigned if present. The remaining sgRNAs with missense annotations were then analyzed for subsequent computational library design.

Three variant effect prediction models, ESM-2 (ref. 66), GEMME[63] and TranceptEVE[65], and an evolutionary conservation estimation server, ConSurf[62], were used to score each missense mutation. The ESM-2 model with 36 layers (esm2_t36_3B_UR50D) was used with the 'masked-marginals' strategy with adjustments to incorporate multiple mutations. GEMME was accessed via its webserver (http://www.lcqb.upmc.fr/GEMME) in single-sequence mode. For TranceptEVE, a single EVE model[101] was trained using the multiple sequence alignment downloaded from the GEMME server without position-specific filtering, and the pretrained Tranception Large model[102] was used. The single-amino-acid substitution scores were summed to produce a score for multiple substitutions, following the scoring strategy of GEMME. A missense score for each sgRNA was then calculated as the weighted sum of predicted variant effect scores, using bystander probabilities from BE-Hive as the weight coefficients. This missense score was used to rank sgRNAs within each model. A combined rank score (LASER score) that incorporated all four models was generated by standardizing and averaging the missense scores across the models.

To assess sgRNA library size versus hit coverage, sgRNAs were selected sequentially from highest to lowest rank, and the proportion of hits covered by the selected sgRNAs was calculated. Hits were defined as those sgRNAs whose z scores were below −1.96, where z scores were calculated from the mean and standard deviation of LFC across all sgRNAs in each screening.

For sgRNA library design, the principal isoform of each target gene was selected based on the APPRIS database[103]. Candidate sgRNAs were then evaluated using LASER, and missense sgRNAs within the top ~20% of LASER scores were selected. We additionally incorporated sgRNAs predicted to target splice sites or introduce premature stop codons for each gene. All sgRNAs were further filtered using BLAT to ensure a single perfect genomic match, thereby minimizing potential off-target activity.

AlphaFold prediction and protein structure visualization

Structural predictions for mouse BRD4–H3K14ac interactions and mouse SMARCA4 structure were performed using the AlphaFold server powered by AlphaFold 3 (ref. 104) with default settings. For mouse ADAR1, the dsRNA binding structure was predicted using the preferred human ADAR1 dsRNA sequence from previous studies[105]. The zinc ion binding sites and inositol hexakisphosphate in the core catalytic domain were aligned based on the human ADAR2 catalytic domain crystal structure (PDB 1ZY7 and 5HP2)[86,106]. The cryo-electron microscopy structure of human ADAR1 in complex with dsRNA derived from the human *GLI1* gene was used as a reference (PDB 9B83)[87]. PyMOL was used to visualize and annotate the structures, with residues colored according to LFC values from screening data.

Primary human T cell activation and culture

Primary human T cells from healthy donors were thawed on day 0 and activated using a 2:1 CD3/CD28 Dynabead (Gibco, 11141D):T cell ratio. Cells were expanded in advanced RPMI-1640 (Gibco, 12633012) supplemented with 10% FBS, 1× penicillin/streptomycin, 10 mM HEPES and 100 IU ml^{-1} recombinant human interleukin-2 (Peprotech, 200-02-50UG). On day 1, T cells were transduced with lentivirus[107]. In short, concentrated lentivirus was loaded onto retronectin-coated plates by centrifugation at 32 °C for 2 h at 2,500*g*. After loading, supernatants were removed, and T cells were added at a density of 1×10^6 cells per ml. On day 4, activation beads were removed from culture using a Dynamag separation magnet (Invitrogen, 12301D). Cells were passaged every 2–3 days in culture to maintain a density of ~1×10^6 cells per ml. For split BE induction experiments, a single dose of 1 nM Rap was added to the culture, followed by flow cytometric analysis of HLA expression after 4 days. The antibody used is BV421 HLA-ABC clone G46-2.6 (BD Biosciences, 565332).

Reporting summary

Further information on research design is available in the Nature Portfolio Reporting Summary linked to this article.

Data availability

High-throughput RNA-seq data are deposited at the Gene Expression Omnibus database (accession number GSE316050)[108]. Source data are provided with this paper.

Code availability

The computational pipeline for LASER is available at https://github.com/kkyamada/laser.

References

90. Chen, S., Zhou, Y., Chen, Y. & Gu, J. fastp: an ultra-fast all-in-one FASTQ preprocessor. *Bioinformatics* **34**, i884–i890 (2018).
91. Dobin, A. et al. STAR: ultrafast universal RNA-seq aligner. *Bioinformatics* **29**, 15–21 (2013).
92. Danecek, P. et al. Twelve years of SAMtools and BCFtools. *Gigascience* **10**, giab008 (2021).
93. Liao, Y., Smyth, G. K. & Shi, W. featureCounts: an efficient general purpose program for assigning sequence reads to genomic features. *Bioinformatics* **30**, 923–930 (2014).
94. Love, M. I., Huber, W. & Anders, S. Moderated estimation of fold change and dispersion for RNA-seq data with DESeq2. *Genome Biol.* **15**, 550 (2014).
95. Kluesner, M. G. et al. EditR: a method to quantify base editing from Sanger sequencing. *CRISPR J.* **1**, 239–250 (2018).
96. Clement, K. et al. CRISPResso2 provides accurate and rapid genome editing sequence analysis. *Nat. Biotechnol.* **37**, 224–226 (2019).
97. Li, W. et al. MAGeCK enables robust identification of essential genes from genome-scale CRISPR/Cas9 knockout screens. *Genome Biol.* **15**, 554 (2014).
98. Gabrielsen, O. S., Sentenac, A. & Fromageot, P. Specific DNA binding by c-Myb: evidence for a double helix-turn-helix-related motif. *Science* **253**, 1140–1143 (1991).
99. Sun, T. et al. ADAR1 editing is necessary for only a small subset of cytosolic dsRNAs to evade MDA5-mediated autoimmunity. *Nat. Genet.* **57**, 3101–3111 (2025).
100. Zeng, T. & Li, Y. I. Predicting RNA splicing from DNA sequence using Pangolin. *Genome Biol.* **23**, 103 (2022).
101. Frazer, J. et al. Disease variant prediction with deep generative models of evolutionary data. *Nature* **599**, 91–95 (2021).
102. Notin, P. et al. Tranception: protein fitness prediction with autoregressive transformers and inference-time retrieval. In *Proc. 39th International Conference on Machine Learning* (eds Chaudhuri, K. et al.) 16990–17017 (PMLR, 2022).
103. Rodriguez, J. M. et al. APPRIS 2017: principal isoforms for multiple gene sets. *Nucleic Acids Res.* **46**, D213–D217 (2018).
104. Abramson, J. et al. Accurate structure prediction of biomolecular interactions with AlphaFold 3. *Nature* **630**, 493–500 (2024).
105. Bahn, J. H. et al. Genomic analysis of ADAR1 binding and its involvement in multiple RNA processing pathways. *Nat. Commun.* **6**, 6355 (2015).
106. Matthews, M. M. et al. Structures of human ADAR2 bound to dsRNA reveal base-flipping mechanism and basis for site selectivity. *Nat. Struct. Mol. Biol.* **23**, 426–433 (2016).
107. Doan, A. E. et al. FOXO1 is a master regulator of memory programming in CAR T cells. *Nature* **629**, 211–218 (2024).
108. Ren, D. et al. High-efficiency small-molecule controlled base editing for in vivo cancer functional genomics. *Gene Expression Omnibus* https://www.ncbi.nlm.nih.gov/geo/query/acc.cgi?acc=GSE316050 (2026).

Acknowledgements

K.Y. acknowledges support from Toyota Riken Overseas Scholarship. C.R.V. acknowledges support from the NIH/NCI R01-CA281106. A.J.M. acknowledges support from the Mark Foundation for Cancer Research. R.M.K. acknowledges support from NIH/NIGMS R01-GM138908. J.S. acknowledges support from NIH/NCI R01-CA258904, the St. Jude Children's Research Hospital Collaborative Research Consortium on Novel Gene Therapies for Sickle Cell Disease and the Mark Foundation for Cancer Research.

Author contributions

D.R., S.W., R.M.K., A.J.M. and J.S. conceived and designed the research. D.R. performed most of the experiments and analyzed the data. S.W. performed in vivo genetic screening and validation experiments. K.Y. developed the LASER pipeline. D.R., K.Y. and Y. Lan developed the sgRNA annotation pipeline. D.R., Y. Lan, S.Z. and R.L. analyzed RNA off-target editing and RNA-seq data. Y. Liu prepared deep sequencing libraries. Y. Liu and C.Z. performed competition assays. R.H. performed primary T cell base editing experiments. A.A. performed the in vitro MYB biochemical experiments. Y.H. performed the in vitro *Adar1* validation experiments. J.P.M. assisted with in vivo experiments. K.N.B. provided resources. Y. Li assisted with data analysis. E.W.W., Q.L., C.R.V., A.J.M., R.M.K. and J.S. supervised the research. A.J.M., R.M.K. and J.S. were responsible for funding acquisition. D.R., R.M.K. and J.S. drafted and edited the paper with input from all authors. All authors read and approved the final paper.

Competing interests

C.R.V. has received consulting fees from Flare Therapeutics, Roivant Sciences and C4 Therapeutics; has served on the advisory boards of

KSQ Therapeutics, Syros Pharmaceuticals and Treeline Biosciences; has received research funding from Boehringer-Ingelheim and Treeline Biosciences and owns a stock option from Treeline Biosciences. A.J.M. is a project member of the Parker Institute for Cancer Immunotherapy and has received research funding from Merck. He has also received honoraria and travel support from Merck, AstraZeneca and Pfizer. He is a scientific consultant for Takeda, Xilio, H3 Biomedicine and Related Sciences. A.J.M. is an inventor on patents related to the IFN pathway and on a filed patent related to modified chimeric antigen receptor T cells. R.M.K. is on the Scientific Advisory Board for Life Edit. The University of Pennsylvania has filed patents on seBEs with J.S., R.M.K. and K.N.B. as inventors.

Additional information

Supplementary information The online version contains supplementary material available at https://doi.org/10.1038/s41587-026-03077-5.

Correspondence and requests for materials should be addressed to Andy J. Minn, Rahul M. Kohli or Junwei Shi.

Peer review information *Nature Biotechnology* thanks Marina Pajic and the other, anonymous, reviewer(s) for their contribution to the peer review of this work.

nature portfolio

Corresponding author(s): NBT-RA65995

Last updated by author(s): Feb 17, 2026

Reporting Summary

Nature Portfolio wishes to improve the reproducibility of the work that we publish. This form provides structure for consistency and transparency in reporting. For further information on Nature Portfolio policies, see our Editorial Policies and the Editorial Policy Checklist.

Statistics

For all statistical analyses, confirm that the following items are present in the figure legend, table legend, main text, or Methods section.

n/a	Confirmed
☐	☒ The exact sample size (*n*) for each experimental group/condition, given as a discrete number and unit of measurement
☐	☒ A statement on whether measurements were taken from distinct samples or whether the same sample was measured repeatedly
☐	☒ The statistical test(s) used AND whether they are one- or two-sided *Only common tests should be described solely by name; describe more complex techniques in the Methods section.*
☒	☐ A description of all covariates tested
☒	☐ A description of any assumptions or corrections, such as tests of normality and adjustment for multiple comparisons
☐	☒ A full description of the statistical parameters including central tendency (e.g. means) or other basic estimates (e.g. regression coefficient) AND variation (e.g. standard deviation) or associated estimates of uncertainty (e.g. confidence intervals)
☐	☒ For null hypothesis testing, the test statistic (e.g. *F*, *t*, *r*) with confidence intervals, effect sizes, degrees of freedom and *P* value noted *Give P values as exact values whenever suitable.*
☒	☐ For Bayesian analysis, information on the choice of priors and Markov chain Monte Carlo settings
☒	☐ For hierarchical and complex designs, identification of the appropriate level for tests and full reporting of outcomes
☒	☐ Estimates of effect sizes (e.g. Cohen's *d*, Pearson's *r*), indicating how they were calculated

Our web collection on statistics for biologists contains articles on many of the points above.

Software and code

Policy information about availability of computer code

Data collection	Millipore Guava easyCyte HT, Beckman CytoFLEX Flow Cytometer, BD FACSAria Fusion sorter, BD FACSJazz sorter, BD LSR II, Illumina NextSeq 550 and 2000, Agilent Bioanalyzer, Thermo Fisher Qubit, Applied Biosystems QuantStudio 6 Pro Real-Time PCR System, and LI-COR Odyssey Imagers
Data analysis	FlowJo v10, GraphPad Prism v10.6.1, fastp v1.0.1, STAR v2.7.1a, featureCounts subread v2.0.3, DESeq2, iBE pipeline, minimap2 v2.30, Image Studio v6.1, ImageJ v1.54g, EditR, CRISPResso2, Snapgene v8.2.1 and PyMOL

For manuscripts utilizing custom algorithms or software that are central to the research but not yet described in published literature, software must be made available to editors and reviewers. We strongly encourage code deposition in a community repository (e.g. GitHub). See the Nature Portfolio guidelines for submitting code & software for further information.

Data

Policy information about availability of data

All manuscripts must include a data availability statement. This statement should provide the following information, where applicable:

- Accession codes, unique identifiers, or web links for publicly available datasets
- A description of any restrictions on data availability
- For clinical datasets or third party data, please ensure that the statement adheres to our policy

The RNA-seq data in this study is available from NCBI Gene Expression Omnibus under accession GSE316050.

The GRCm39/mm39 mouse reference genome is publicly available.
The computational pipeline for LASER will be available at https://github.com/kkyamada/laser.

Research involving human participants, their data, or biological material

Policy information about studies with human participants or human data. See also policy information about sex, gender (identity/presentation), and sexual orientation and race, ethnicity and racism.

Reporting on sex and gender	n/a
Reporting on race, ethnicity, or other socially relevant groupings	n/a
Population characteristics	n/a
Recruitment	n/a
Ethics oversight	n/a

Note that full information on the approval of the study protocol must also be provided in the manuscript.

Field-specific reporting

Please select the one below that is the best fit for your research. If you are not sure, read the appropriate sections before making your selection.

☒ Life sciences ☐ Behavioural & social sciences ☐ Ecological, evolutionary & environmental sciences

For a reference copy of the document with all sections, see nature.com/documents/nr-reporting-summary-flat.pdf

Life sciences study design

All studies must disclose on these points even when the disclosure is negative.

Sample size	For in vitro study, samples from cell lines were evaluated in duplicate, triplicate or quadruplicate. For in vivo study, 5-10 individual mice were used per condition. No sample-size calculations were performed. Sample sizes in all experiments were determined to be sufficient due to effect size, level of variation within groups, consistency of measurable differences among groups, and statistical indicators of reproducibility.
Data exclusions	No data was excluded.
Replication	Biological replicate experiments from cell lines were performed using cells with different passage number spanning days to weeks; Data from in vivo Adar1 tiling screens represent two independent biological replicate experiments with 5-10 individual mice per condition for each replicate; Data from in vivo LASER designed library screens represent one biological replicate experiment with 5-10 individual mice per condition; Flow cytometry analyses were performed on independently harvested tumors from multiple mice per condition, with each mouse shown as individual data points; Western blot were conducted in two independent biological replicates with similar results; RNA-seq experiments were performed on independently prepared biological samples.
Randomization	For in vivo mouse experiments, mice were randomized by cage and littermates. For in vitro studies, random allocation is not relevant.
Blinding	Investigators were not blinded to group allocation during data collection or analysis. Blinding was not relevant to this study because assignment of data values to samples was automated (e.g. flow cytometry and NGS sequencing) and not based on subjective investigator assessments or assigning values from an analog measurement device.

Reporting for specific materials, systems and methods

We require information from authors about some types of materials, experimental systems and methods used in many studies. Here, indicate whether each material, system or method listed is relevant to your study. If you are not sure if a list item applies to your research, read the appropriate section before selecting a response.

Materials & experimental systems

n/a	Involved in the study
☐	☒ Antibodies
☐	☒ Eukaryotic cell lines
☒	☐ Palaeontology and archaeology
☐	☒ Animals and other organisms
☒	☐ Clinical data
☒	☐ Dual use research of concern
☒	☐ Plants

Methods

n/a	Involved in the study
☒	☐ ChIP-seq
☐	☒ Flow cytometry
☒	☐ MRI-based neuroimaging

Antibodies

Antibodies used

c-Myb (D2R4Y) antibody (Cell signaling, cat#12319) 1:1000; BRD4 antibody (Bethyl laboratories, cat#A301-985A) 1:1000; ADAR1 antibody (Santa Cruz, cat#73408) 1:500; Phospho-p70 S6 kinase (T389) antibody (Cell Signaling, #9234) 1:1000; p70 S6 kinase antibody (Cell Signaling, cat#9202) 1:1000; GAPDH (14C10) antibody (Cell Signaling, cat#2118) 1:2000; PKR (Cell Signaling, cat#12297) 1:1000; phosphorylated PKR (phospho-T446, Abcam, cat#ab32036) 1:1000; Goat anti-Rabbit IgG secondary antibody (LI-COR Biosciences, cat#926-32211) 1:10000; Goat anti-Mouse IgG secondary antibody (Invitrogen, cat#A21058) 1:10000; PE/Dazzle™ 594 CD44 clone IM7 (Biolegend, cat#103055) 1:200; APC FoxP3 clone FJK-16s (eBioscience, cat#17-5773-82) 1:100; Alexa Fluor® 700 CD45.2 clone 104 (BioLegend, cat#109822) 1:200; APC-eFluor™ 780 NK1.1 clone PK136 (eBioscience, cat#47-594-82) 1:200; FITC Granzyme B clone GB11 (BioLegend, cat#515403) 1:100; PerCP/Cyanine5.5 CD4 clone RM4-5 (BioLegend, cat#100540) 1:200; Brilliant Violet 605™ B220 clone RA3-6B2 (BioLegend, cat#103243) 1:200; Brilliant Violet 650™ CD8a clone 53-6.7 (BioLegend, cat#100742) 1:200; Brilliant Violet 785™ CD3 clone 17A2 (BioLegend, cat#100232) 1:200; Alexa Fluor® 647 F4/80 clone BM8 (BioLegend, cat#123121) 1:200; APC-eFluor™ 780 B220 clone RA3-6B2 (eBioscience, cat#47-0452-82) 1:200; APC/Cyanine7 CD3 clone 17A2 (BioLegend, cat#100221) 1:200; Brilliant Violet 711™ Ly6C clone HK1.4 (BioLegend, cat#128037) 1:200; PE CD11b clone M1/70 (BD Biosciences, cat#553311) 1:200; PE/Dazzle™ 594 CD11c clone N418 (BioLegend, cat#117347) 1:200; PE/Cyanine5 I-A/I-E (MHC-II) clone M5/114.15.2 (BioLegend, cat#107612) 1:200; PE-Cy™7 Ly6G clone 1A8 (BD Biosciences, cat#560601) 1:200; BV421 HLA-ABC clone G46-2.6 (BD Biosciences, cat#565332) 1:400.

Validation

All antibodies listed above have been used and cited by other researchers as shown in manufacturer's website.
c-Myb antibody, BRD4 antibody, and ADAR1 antibody were validated by Western Blot using target gene KO cells generated by seBE editing in this study.
For p70 S6 kinase and phospho-p70 S6 kinase (Thr389), specificity was validated by rapamycin treatment, which resulted in the expected reduction of Thr389 phosphorylation without affecting total p70 S6 kinase levels. PKR and phospho-PKR (Thr446) antibodies were validated by interferon-β (IFN-β) stimulation, which led to increased PKR phosphorylation.
GAPDH antibody was validated by Western Blot, a single band showed at the indicated molecular weight (~34KDa).
Flow cytometry antibodies were validated by staining cells with both positive and negative populations.

Eukaryotic cell lines

Policy information about cell lines and Sex and Gender in Research

Cell line source(s)	RN2, HEK293T, B16-F10 cells were cultured in house
Authentication	None of the cell lines used were authenticated.
Mycoplasma contamination	All the cell lines were tested as mycoplasma negative.
Commonly misidentified lines (See ICLAC register)	No cell line used is in the database.

Animals and other research organisms

Policy information about studies involving animals; ARRIVE guidelines recommended for reporting animal research, and Sex and Gender in Research

Laboratory animals	5- to 7-week-old female C57BL/6 mice were obtained from Charles River Laboratory, maintained under specific pathogen-free conditions on a 12-hour light/12-hour dark cycle at 20–26°C and 30–70% relative humidity, and randomly assigned to experimental groups.
Wild animals	No wild animal is involved in the study.
Reporting on sex	Sex was not considered in the study.
Field-collected samples	Field-collected sample is not involved in the study.
Ethics oversight	All animal experiments were conducted in accordance with protocols approved by the Institutional Animal Care and Use Committee of the University of Pennsylvania.

Note that full information on the approval of the study protocol must also be provided in the manuscript.

Plants

Seed stocks	n/a
Novel plant genotypes	n/a
Authentication	n/a

Flow Cytometry

Plots

Confirm that:

☒ The axis labels state the marker and fluorochrome used (e.g. CD4-FITC).

☒ The axis scales are clearly visible. Include numbers along axes only for bottom left plot of group (a 'group' is an analysis of identical markers).

☒ All plots are contour plots with outliers or pseudocolor plots.

☒ A numerical value for number of cells or percentage (with statistics) is provided.

Methodology

Sample preparation	For in vitro cell lines, cells were either directly analyzed by a Guava easyCyte HT and Beckman CytoFLEX Flow Cytometer, or resuspened in FACS buffer (PBS supplemented with 5% FBS) for cell sorting. For tumor immune infiltration studies, single-cell suspensions of tumors were prepared, and red blood cells were lysed using ACK Lysis Buffer. Cells were stained with antibodies and resuspended in FACS buffer for flow cytometry analysis. For in vivo screens, single-cell suspensions were treated with ACK Lysis Buffer and resuspended in FACS buffer for flow cytometry analysis. For primary human T cell editing experiments, T cells were activated for 4 days and passaged every 2-3 days in culture to maintain a density of approximately 1×10^6 cells mL^{-1}. A single dose of 1nM rapamycin was added, and cells were stained and analyzed by flow cytometry analysis 4 days after treatment.
Instrument	Millipore Guava easyCyte HT, Beckman CytoFLEX Flow Cytometer, BD FACSAria Fusion sorter, BD FACSJazz sorter, BD LSR II
Software	FlowJo v10
Cell population abundance	The purity of sorted cell population was >90%, which was determined by Guava easyCyte HT post sorting.
Gating strategy	For in vitro cell line experiments, live cells were gated based on FSC-A/SSC-A, and mCherry +/- populations or GFP +/- populations were analyzed. For analysis of in vitro CD44 editing, seBE+ sorted B16-F10 cells were stained with CD44 antibody and CD44+/- populations were quantified. For tumor immune infiltration analysis, live/dead cell discrimination was performed using the Live/Dead Fixable Aqua Dead Cell Stain Kit. Total immune cells were identified as CD45+, NK cells as NK1.1+CD3-, total T cells as NK1.1-CD3+, regulatory T cells (Tregs) as CD4+FOXP3+, dendritic cells as CD11b+CD11c+MHCII+, tumor-associated neutrophils (TANs) as CD11b+Ly6G +Ly6C+, macrophages as F4/80+CD11b+, and monocytes as $CD11b^{+}Ly6C^{+}$. For in vivo screens, GFP+ cells were quantified as sgRNA+ cells. For primary human T cell editing experiments, cells were gated for singlets and GFP+ cells were identified as sgRNA+. Surface HLA expression was assessed by flow cytometry to quantify B2M knockout efficiency.

☒ Tick this box to confirm that a figure exemplifying the gating strategy is provided in the Supplementary Information.